Climate Dynamics (2003) 20: 127–151
DOI 10.1007/s00382-002-0260-x

S.-I. Shin · Z. Liu · B. Otto-Bliesner · E.C. Brady
J.E. Kutzbach · S.P. Harrison

A Simulation of the Last Glacial Maximum climate using the NCAR-CCSM

Received: 7 June 2001 / Accepted: 10 April 2002 / Published online: 5 July 2002

Abstract The National Center for Atmospheric Research-Community Climate System Model (NCAR-CCSM) is used in a coupled atmosphere–ocean–sea-ice simulation of the Last Glacial Maximum (LGM, around 21,000 years ago) climate. In the tropics, the simulation shows a moderate cooling of 3 °C over land and 2 °C in the ocean in zonal average. This cooling is about 1 °C cooler than the CLIMAP sea surface temperatures (SSTs) but consistent with recent estimates of both land and sea surface temperature changes. Subtropical waters are cooled by 2–2.5 °C, also in agreement with recent estimates. The simulated oceanic thermohaline circulation at the LGM is not only shallower but also weaker than the modern with a migration of deep-water formation site in the North Atlantic as suggested by the paleoceanographic evidences. The simulated northward flow of Antarctic Bottom Water (AABW) is enhanced. These deep circulation changes are attributable to the increased surface density flux in the Southern Ocean caused by sea-ice expansion at the LGM. Both the Gulf Stream and the Kuroshio are intensified due to the overall increase of wind stress over the subtropical oceans. The intensified zonal wind stress and southward shift of its maximum in the Southern Ocean effectively enhances the transport of the Antarctic Circumpolar Current (ACC) by more than 50%. Simulated SSTs are lowered by up to 8 °C in the midlatitudes. Simulated conditions in the North Atlantic are warmer and with less sea-ice than indicated by CLIMAP again, in agreement with more recent estimates. The increased meridional SST gradient at the LGM results in an enhanced Hadley Circulation and increased midlatitude storm track precipitation. The increased baroclinic storm activity also intensifies the meridional atmospheric heat transport. A sensitivity experiment shows that about half of the simulated tropical cooling at the LGM originates from reduced atmospheric concentrations of greenhouse gases.

1 Introduction

Since the pioneering efforts of the CLIMAP project members (1976, 1981), the understanding of the climate of the LGM has been an important challenge confronting the climate community. With ongoing concerns about climate change due to increasing greenhouse gases (IPCC WG-I 1996), the study of past climate plays a unique role in understanding both the natural variability of the climate system and model sensitivity to climatic perturbations.

Most simulations of the LGM climate to date have been made with stand-alone atmospheric or oceanic general circulation models. In these simulations, the lower (upper) boundary of the atmosphere (ocean) is prescribed. Two approaches are usually adopted in atmospheric general circulation models. One is prescribing global observed or reconstructed SSTs (Gates 1976; Manabe and Hahn 1977; Kutzbach and Wright 1985; Rind and Peteet 1985; Kutzbach and Guetter 1986; Hall et al. 1996; Crowley and Baum 1997; Dong and Valdes 1998), the other is prescribing oceanic heat transport with a mixed-layer ocean to mimic the effect of SST feedback on the climate system (Hewitt and Mitchell 1997; Webb et al. 1997; Dong and Valdes 1998; Broccoli 2000).

S.-I. Shin (✉) · Z. Liu · J.E. Kutzbach
Center for Climatic Research and
Department of Atmospheric and Oceanic Sciences,
1225 W Dayton st.,
University of Wisconsin-Madison,
Madison, Wisconsin, 53706-1695, USA
E-mail: shin@ocean.meteor.wisc.edu

B. Otto-Bliesner · E.C. Brady
National Center for Atmospheric Research,
Boulder, Colorado, USA

S.P. Harrison
Max Planck Institute for Biogeochemistry,
Jena, Germany

Despite a major increase in the number of marine records available over the last two decades, CLIMAP (1981) remains the only data set describing SST patterns on a global grid. However, recent work shows that there are substantial problems with this gridded data set both in the tropics and in the North Atlantic. Specifically, CLIMAP estimates of tropical SSTs are too warm in the Coral Sea (Anderson et al. 1989), the tropical Atlantic Ocean (Guilderson et al. 1994; Zhao et al. 1995; Chapman et al. 1996; Wolff et al. 1998; Mix et al. 1999), the subtropical and tropical Pacific Ocean (Ohkouchi et al. 1994; Prahl et al. 1995; Patrick and Thunell 1997; Lee and Slowey 1999) and the tropical Indian Ocean (Bard et al. 1997; Sonzogni et al. 1997). Atmosphere-only simulations using prescribed CLIMAP SSTs are intrinsically constrained by the imposed boundary conditions and this results in substantial discrepancies between simulated and observed temperature changes over the land in the tropics (see e.g., Pinot et al. 1999a). A large part of this disagreement between simulated and observed tropical climates results from the interpolation techniques used by CLIMAP (1981) in regions of the tropical oceans where the ocean data coverage was poor (Broccoli and Marciniak 1996). Simulations in which the CLIMAP SSTs are globally lowered by 2 °C (e.g., Rind and Peteet 1985) result in a tropical cooling that is more consistent with data-based estimates of the LGM cooling. Similarly, at least some simulations made with a mixed-layer ocean within the Palaeoclimate Modelling Intercomparison Project (PMIP: Pinot et al. 1999a) appear to be able to produce tropical cooling consistent with both marine and terrestrial observations.

The discrepancies between CLIMAP and more recent reconstructions of ocean conditions in the North Atlantic pose a more fundamental problem. Reconstructions based on foraminiferal test (Weinelt et al. 1996) and dinoflagellate cyst (de Vernal et al. 1997, 2000; Rochon et al. 1998) assemblages suggest that the seasonal cycle of SSTs in the North Atlantic was considerably larger than shown by CLIMAP (1981), and that large areas of the Greenland–Iceland–Norwegian (GIN) seas assumed to have been ice-covered throughout the year in the CLIMAP data set were ice-free in summer. Sensitivity experiments made using the Weinelt et al. (1996) data set indicate that the reduced sea-ice cover and warmer SSTs in summer weaken the zonal circulation over Europe and northern Eurasia (Joussaume et al. 1999; Pinot et al. 1999b). Simulations that only take into account the thermal response of the ocean and neglect dynamical changes cannot reproduce the large seasonal shifts in sea-ice limits and ocean temperatures in the North Atlantic shown by the most recent reconstructions of ocean conditions (see e.g., Kageyama et al. 2001). This provides a strong motivation, in the absence of a revised global data set of SSTs, to use dynamical ocean models.

Ocean-only simulations of the LGM are driven by prescribing the momentum, heat, and freshwater fluxes into the ocean. Global reconstructions of these fluxes do not exist, and therefore the ocean simulations made to date have either used estimates derived from atmospheric simulations or have used restoration techniques to mimic the fluxes. Thus, the majority of the LGM ocean simulations have used momentum flux (wind stress) estimates based upon the output of atmospheric simulations of the LGM (Lautenschlager et al. 1992; Seidov et al. 1996; Seidov and Haupt 1997; Bigg et al. 1998; Winguth et al. 1999). Most ocean models have used CLIMAP SSTs as a restoring boundary condition for heat flux. Freshwater fluxes have been derived from the output of LGM atmospheric simulations (Lautenschlager et al. 1992). Alternatively, in limited regions where there are data-based reconstructions of LGM salinity (e.g., Duplessy et al. 1991), surface salinity is restored to mimic the freshwater flux (Seidov et al. 1996; Seidov and Haupt 1997). Inverse methods have also been used to infer the global salinity pattern of the LGM based on reconstructed paleonutrient distributions linked to the LGM overturning circulation in the ocean (Winguth et al. 1999). None of these methods is entirely reliable. The known problems with the CLIMAP data set mean that use of these SST reconstructions either directly as a restoring boundary condition or indirectly through prescribing ocean conditions in the atmospheric simulations is problematic. The alternative approaches of using sea surface salinity (SSS) or paleonutrient reconstructions are based on relatively little data and are therefore poorly constrained.

The use of coupled atmosphere–ocean models provides a way to avoid the deficiencies in the LGM simulations of atmosphere or ocean alone (e.g., Ganopolski et al. 1998; Weaver et al. 1998; Bush and Philander 1998; 1999; Hewitt et al. 2001; Kitoh et al. 2001). In this study, we use a coupled atmosphere–ocean–sea-ice model, the NCAR-CCSM (Boville and Gent 1998), integrated for a long enough period (110 years, after a long spin-up of each component) to ensure statistical reliability, to investigate the climate and the tendency of the oceanic overturning circulation at the LGM.

2 The NCAR-CCSM model

The NCAR-CCSM version 1.4 is used to simulate the climate of the LGM without any flux adjustment. The coupled model consists of four independent components representing the atmosphere, ocean, sea-ice, and land surface. Each component of the model communicates with each other part through a flux coupler. While the ocean component communicates at a daily interval, the atmosphere, land surface, and sea-ice components communicate at an hourly interval.

The atmospheric component of the model, the Community Climate Model (CCM; Kiehl et al. 1998) version 3.6, employs spectrally truncated T31 grid resolution (~3.75°) in the horizontal with 18 vertical levels. Besides CO_2, the model includes the radiative effects of CH_4, N_2O, CFC-11 and CFC-12. The radiative forcing contributions of various greenhouse gases to the LGM climate will be discussed later. The land surface model (LSM; Bonan 1998) calculates surface fluxes and soil moisture content but employs prescribed vegetation types.

The ocean component, the NCAR-CCSM Ocean Model (NCOM; Gent et al. 1998), has non-uniform horizontal and vertical grid resolutions (hereafter referred to as ×3′ resolution). The horizontal grid increases from 0.8° latitude on the equator to 1.85° at the poles, although the grid is a uniform 3.6° in longitude. There are 25 non-uniform grid boxes vertically, with the smallest (12 m thick) at the surface and the largest (450 m thick) at depth. The Gent-McWilliams eddy mixing parameterization (Gent and McWilliams 1990; Gent et al. 1995) is used in the horizontal tracer equations. Vertically, the non-local K-profile boundary layer mixing parameterization of Large et al. (1994) is incorporated with a background-mixing coefficient of 1.5×10^{-5} m^2·s^{-1}. A deep ocean acceleration technique (Bryan 1984) is applied during the ocean spin-up integrations to obtain a quasi-equilibrium state of oceanic overturning circulation.

The sea-ice component, the NCAR-CCSM Sea-Ice Model (CSIM; Weatherly et al. 1998), consists of a three-layer thermodynamic sea-ice model, based upon Semtner (1976), and a cavitating fluid dynamic sea-ice model (Flato and Hilber 1992) applied at the same resolution as NCOM.

Instead of using a river runoff model, due to the uncertainty of river systems at the LGM, we incorporate a simple precipitation-scaling scheme (Boville and Gent 1998) to ensure the conservation of freshwater in the coupled model.

3 Experimental design and coupling procedures

3.1 Boundary conditions

The orbital parameters, eccentricity, obliquity and the longitude of perihelion are set to the LGM values (Berger 1978; Table 1). The height and the extent of ice-sheets are interpolated from the paleotopography map of Peltier (1994). The ocean depth is uniformly reduced by 105 m so that modern continental shelves shallower than 105 m are exposed. Currently available maps of vegetation distribution at the LGM (e.g., Adams and Faure 1997; Crowley and Baum 1997) are not consistent with site-based vegetation reconstructions based on pollen and/or plant macrofossil data (Prentice et al. 2000). We simply used the modern vegetation distributions (except in the regions covered by ice-sheets). The vegetation of the continental shelf freshly exposed at the LGM is assigned by averaging the modern vegetation types of the nearest points. The change of ocean salinity due to the presence of the large fresh-water ice-sheets is taken into account by increasing the salinity in the ocean by 1 psu (practical salinity unit). The concentrations of CO_2, CH_4, and N_2O are lowered to the values reconstructed from Greenland and Antarctic ice cores (Table 1; Raynaud et al. 1993). The reduction of CO_2 from 280 ppmv (pre-industrial concentration) to 200 ppmv results in a radiative forcing change of –1.8 W·m^{-2} compared to the pre-industrial era (Fig. 1). The change in CH_4 and N_2O results in a further –0.7 W·m^{-2} change in forcing. Thus, the total LGM radiative forcing change due to reduction of greenhouse gases is –2.5 W·m^{-2}, which is comparable to previous calculations (Hoffert and Covey 1992; Hansen et al. 1993). In addition to the reduced greenhouse gases, it is also suggested that the presence of ice-sheets also causes the radiative forcing change comparable to the reduced greenhouse gas forcing at the LGM (Hewitt and Mitchell 1997; Broccoli 2000).

Table 1 Orbital parameters (Berger 1978) and greenhouse gas concentrations (Raynaud et al. 1993) used for the modern and the LGM simulations. The numbers in parentheses represent the pre-industrial concentrations of greenhouse gases

	MODERN	LGM
Orbital parameters		
Eccentricity	0.016724	0.018994
Obliquity	23.446°	22.949°
Longitude of perihelion	102.04°	114.42°
Greenhouse gases (ppm)		
CO_2	354.4(280.0)	200
CH_4	1.722(0.800)	0.35
N_2O	0.308(0.288)	0.19
CFC-11	0.51×10^{-3}(0)	0
CFC-12	0.46×10^{-3}(0)	0

3.2 Coupling procedures

Combinations of the model components are integrated separately to obtain an appropriate initial state of the coupled system prior to full coupling (Fig. 2, Table 2). The atmospheric model, CCM3/LSM, with thermodynamic sea-ice (CISM) is integrated for 10 model years with observed SSTs (Shea et al. 1990) for the modern atmosphere control (A-CTL) and with CLIMAP SSTs (CLIMAP

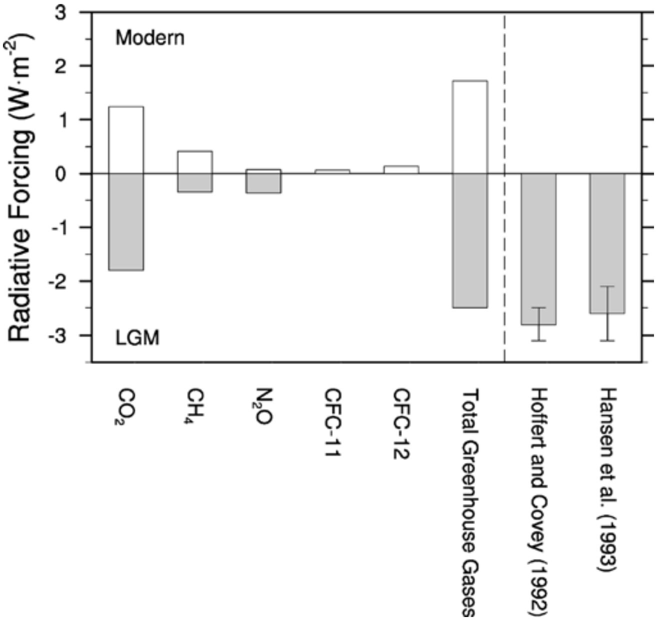

Fig. 1 The radiative forcing (W·m^{-2}) of greenhouse gases, CO_2, CH_4, N_2O, CFC-11 and CFC-12, today and at the LGM relative to pre-industrial levels. The calculations of radiative forcing follow IPCC WG-I (1996), i.e. the radiative forcing of CO_2, CH_4, N_2O, CFC-11 and CFC-12 are

$$CO_2 = 5.35 \times \ln \frac{C}{C_0}$$

$$CH_4 = 0.036 \times \left(\sqrt{M} - \sqrt{M_0}\right) - (\chi(M, N_0) - \chi(M_0, N_0))$$

$$N_2O = 0.120 \times \left(\sqrt{N} - \sqrt{N_0}\right) - (\chi(M_0, N) - \chi(M_0, N_0))$$

$$CFC - 11 = 0.22 \times X$$

$$CFC - 12 = 0.28 \times Y$$

where C, M, N, X and Y are the concentrations of CO_2, CH_4, N_2O, CFC-11 and CFC-12 respectively; C_0, M_0 and N_0 are the equivalent pre-industrial concentrations of CO_2, CH_4 and N_2O, and

$$\chi(a, b) = 0.47 \times \ln\left(1 + 2.01 \times e^{-5 \times (a \times b)^{0.75}} + 5.31 \times e^{-15 \times a \times (a \times b)^{1.53}}\right).$$

Radiative forcing inferred from proxy data at the LGM (Hoffert and Covey 1992; Hansen et al. 1993) are also plotted for comparison

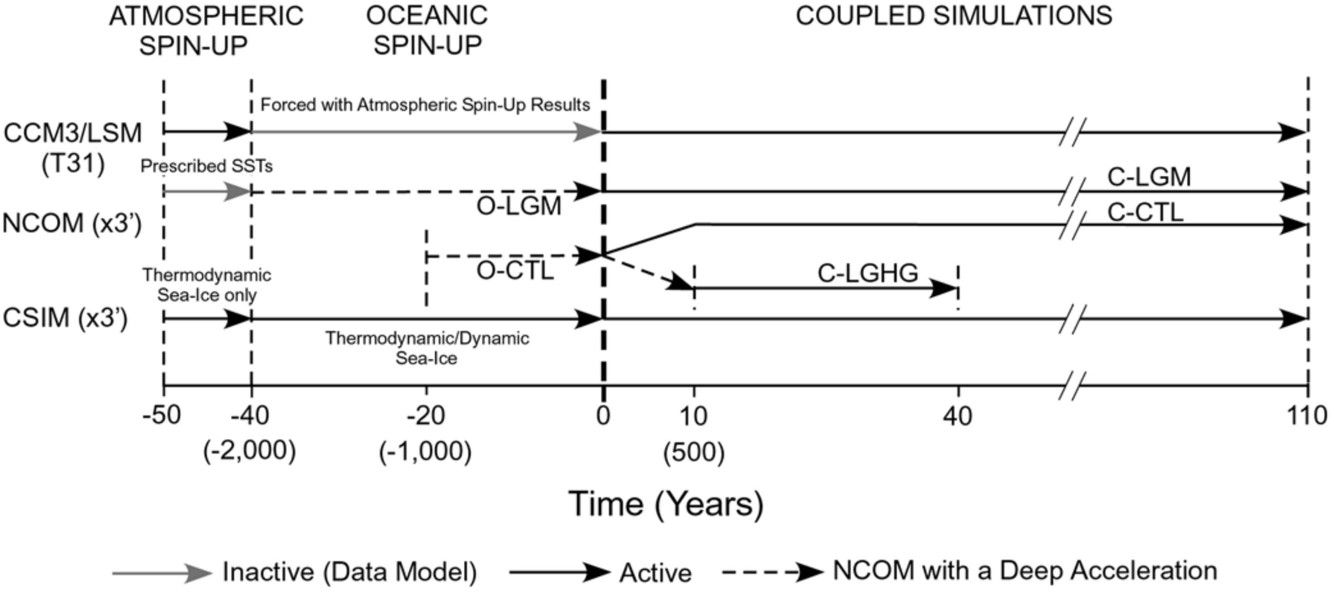

Fig. 2 Schematic diagram of the spin-up and coupling procedures

Table 2 The experiments and boundary conditions. The numbers in parentheses are the averaging periods for the analysis

Experiment name	Land/sea configuration	Orbital parameters	Greenhouse gases	Vegetation types	Integration period (years) (averaging period; years)
Atmospheric spin-up					
A-CTL	Modern	Modern	Modern	Modern	10(5)[a]
A-LGM	LGM	LGM	LGM	Modern + glaciers	10(5)[a]
Oceanic spin-up					
O-CTL	Modern	–	–	–	20[b]
O-LGM	LGM	–	–	–	40[b]
Coupled experiments					
C-CTL	Modern	Modern	Modern	Modern	110(50)
C-LGM	LGM	LGM	LGM	Modern + glaciers	110(50)
C-LGHG	Modern	Modern	LGM	Modern	40(20)[c]

[a] The atmospheric spin-up integration is forced with SSTs from Shea et al. (1990) climatology in A-CTL and from CLIMAP (1981) in A-LGM

[b] The O-CTL (O-LGM) is spun-up using the surface fluxes from the A-CTL (A-LGM) with the deep acceleration technique (Bryan 1984)

[c] The coupled sensitivity test, C-LGHG, starts from a modern ocean state with the deep acceleration technique in the first 10 model years. Then, 30-year integration is performed without the deep acceleration technique

project members 1981) for the LGM atmosphere (A-LGM). The heat, freshwater, and momentum fluxes from the last five-year results of A-CTL and A-LGM are used to drive the oceanic component of the model. The ocean model, NCOM, with CISM (both thermodynamic and dynamic sea-ice components) is spun-up for 20 and 40 surface model years for the modern ocean (O-CTL) and the LGM ocean (O-LGM) respectively. The 20 and 40 surface model years are equivalent to 1000 and 2000 model years in the deep ocean respectively because of the use of a deep acceleration technique (Bryan 1984) during spin-up. The coupled integrations (coupled control, C-CTL, and coupled LGM, C-LGM) are performed for 110 model years without any flux adjustment or deep acceleration. The convergence issue of the coupled LGM simulation will be discussed in Appendix 1.

An alternative LGM simulation started from the modern ocean state (initial state of C-CTL ocean) is also integrated for 300 surface model years with a deep-ocean acceleration, equivalent to 15,000 abyssal model years. The simulated results of two LGM simulations are remarkably close to each other. The comparisons of two LGM simulations will be discussed in Appendix 1.

The sensitivity of the coupled climate model to lowered greenhouse gases alone was also tested (C-LGHG). This integration starts from the initial state of C-CTL and proceeds for 40 model years with the LGM concentrations of greenhouse gases (Table 1).

The results presented here are averaged over the last 50 years in the coupled modern and LGM runs (C-CTL and C-LGM) and over the last 20 years in coupled sensitivity test (C-LGHG).

4 Results

4.1 Sea surface conditions

4.1.1 Temperature and salinity

Despite the fact that the LGM tropical ocean surface gains more heat than the modern (Table 3), a zonal

Table 3 The glacial-modern changes in the surface heat flux (W·m^{-2}) and the freshwater flux (m·yr^{-1}) over the ocean

	>45°S	45°S–15°S	15°S–15°N	15°N–45°N	45°N<
Heat flux change (W·m^{-2})	–4.0	0.9	1.4	–0.1	–13.1
Freshwater flux change (m·yr^{-1})					
P-E	16.3	8.3	–6.3	11.6	–8.1
Ice effect	–25.0				–9.9

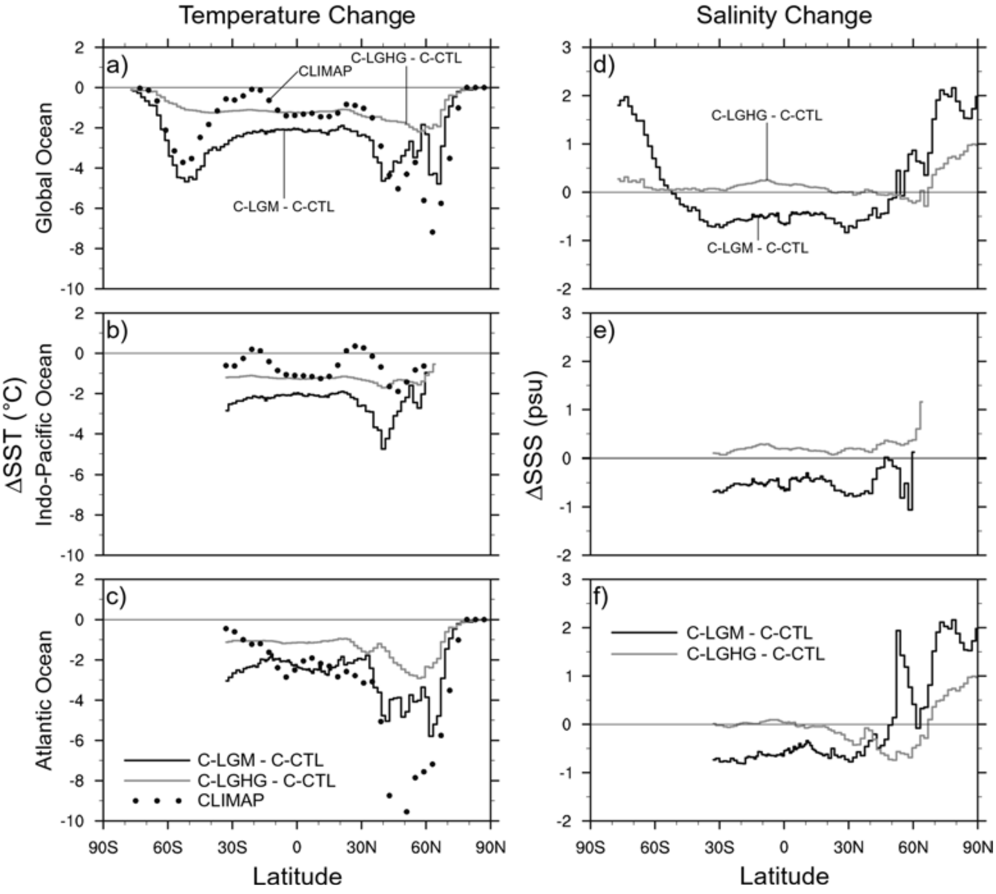

Fig. 3 The differences of zonally averaged annual SST (°C) in the **a** global Ocean, **b** Indo-Pacific Ocean and **c** Atlantic Ocean including the Arctic, for the LGM minus control (C-LGM-C-CTL, *black lines*) and for the LGM greenhouse gas forcing minus control (C-LGHG-C-CTL, *gray lines*). **d**–**f** are the same as **a**–**c**, but for the SSS (psu). The *dots* in **a**–**c** represent the SST differences inferred by CLIMAP (1981)

cooling of 2 °C is simulated in the tropics (Fig. 3a), which is about 1 °C cooler than the CLIMAP SSTs. The largest differences with CLIMAP estimates occur in the tropical Indo-Pacific (Fig. 3b). In the tropical Atlantic, the average of the simulated SST change agrees with the CLIMAP estimates (Fig. 3c), although differences exist in the north–south structure (Fig. 3c). About half of the simulated tropical cooling is caused by reduced greenhouse gases (Fig. 3a–c). In addition to the reduced greenhouse effect, the positive water-vapor feedback contributes to the simulated tropical cooling (Broecker 1995). Figure 4 shows the zonally averaged surface relative humidity, and zonally and vertically averaged specific humidity change in the simulations. Whereas the specific humidity (water content of the atmosphere) is decreased in all latitudinal bands with the largest decrease in the tropics at the LGM (Fig. 4b; see also Fig. 18d), the surface relative humidity shows little change at the LGM, only about 1% decrease in the tropics (Fig. 4a). These humidity changes induce the positive water-vapor feedback in the atmosphere and, in turn, SST cooling in the ocean. Furthermore, it is shown that the LGM cooling in the Southern Ocean by the positive sea-ice-albedo feedback also contributes to the tropical cooling by enhanced ocean ventilation of the thermocline and the intermediate waters (Liu et al. 2001).

The simulations are significantly different from CLIMAP estimates in the subtropics, where the small cooling (or even slight warming in the Indo-Pacific) shown by CLIMAP estimates is replaced by 2–2.5 °C cooling. This cooling is due partly to lowered greenhouse gases and partly to atmosphere–ocean interaction including the export of cold air from the continents, which cools the western oceans. The largest simulated ocean cooling occurs in the mid- and high latitudes near the sea-ice margin, with 5 °C in the North Pacific, 6 °C in the North Atlantic and 5 °C in the Southern Ocean. In the

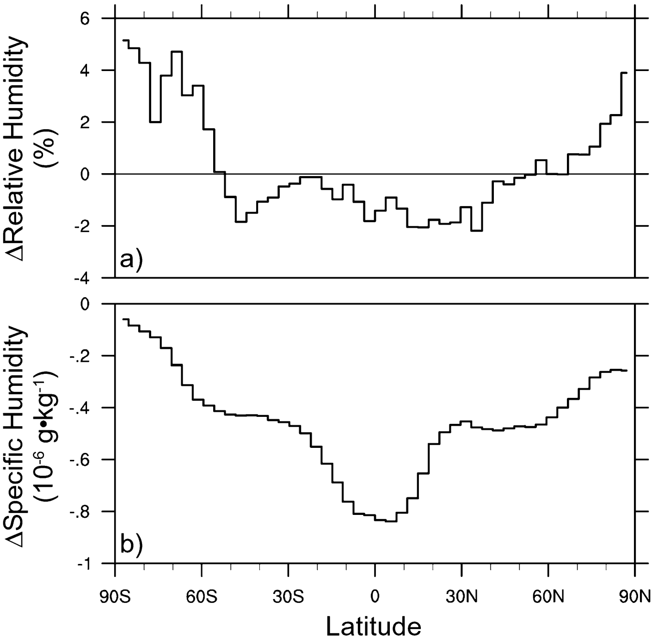

Fig. 4 **a** Zonally averaged glacial-modern surface relative humidity change (%). **b** Zonally and vertically averaged glacial-modern specific humidity change (10^{-6} g·kg^{-1})

mid- and high latitudes, the contribution from reduced greenhouse gases is small except between 50–60°N.

Globally, the latitudinal variation of simulated SST approximately follows CLIMAP reconstructions except between 40–60°N where the simulated cooling is much smaller than CLIMAP estimates. The north–south SST gradient in the tropics is increased slightly in the Southern Hemisphere during the LGM, but remains the same or slightly reduced in the Northern Hemisphere (Fig. 3a). The SST gradient in the midlatitudes in C-LGM is increased compared to C-CTL in both hemispheres (Fig. 3a). These changes in the thermal gradient of the ocean surface impact on atmospheric eddy activity and meridional atmospheric heat transport (as discussed later).

Sea surface salinity, excluding the 1 psu increase due to the presence of ice-sheets (discussed previously), is characterized by ubiquitous freshening (i.e., changes < 1 psu) due to overall increase of freshwater flux (precipitation minus evaporation, *P-E*) anomaly at the LGM (Table 3), except in the sea-ice covered regions (Fig. 3d). The increase in salinity under sea-ice is mainly due to the release of brine during the sea-ice formation in C-LGM (Table 3). In contrast to the SST changes, the contributions of greenhouse gases to the SSS changes are small and even of opposite sign in ice-free regions. In C-LGHG, the SSS is increased in the Indo-Pacific and decreased in the North Atlantic Ocean. But, the opposite change is observable in C-LGM as a zonal average, i.e., a saltier North Atlantic (north of 40°N) and a fresher Indo-Pacific Ocean. This implies that changes of LGM atmospheric circulation caused by something other than greenhouse gases alter the atmospheric hydrological cycle and the interbasin moisture transport. This saltier North Atlantic (north of 40°N) is mainly because of the salinity increase in the south of Greenland and in the Arctic Ocean (see Fig. 5b) by decrease of *P-E* (figure not shown) and the sea-ice thickening (see Fig. 20 and Table 3) respectively. SSS in the North Atlantic between 60–70°N, spanning the part of GIN Seas, is lower than modern (Figs. 3c, 5b). This freshening is caused, in part, by seasonal melting of sea-ice (see Fig. 21). Since this region is one of the formation sites of North Atlantic Deep Water (NADW), it is conceivable that a substantial change of deep-water formation is in progress in the coupled LGM simulations.

Maps of the SST changes (Fig. 5a) confirm the existence of strong north–south SST gradients, with large cooling in mid- to high latitudes and smaller cooling in the tropics, but show that the anomalous east–west SST gradients are relatively weak. For instance, a near uniform cooling of 2 °C is apparent in the equatorial Pacific, although there is a tendency for larger (3 °C) cooling in the far western and smaller (1 °C) cooling in the far eastern equatorial Pacific.

The widespread freshening in the ocean is also evident in the SSS anomaly patterns (Fig. 5b). Away from the sea-ice covered region, the SSS is increased by 2 psu only in the south of Greenland. The freshening is also shown in the modern NADW formation areas, i.e., the Nordic seas. The migration of salty waters indicates that deep-water is being formed south of Greenland at the LGM, and the oceanic mixed-layer depth is increased in this region (see Sect. 4.2.2; Fig. 11a, b). Salinity is also increased in the Antarctic due to increased sea-ice formation at the LGM.

4.1.2 Wind stress

The surface zonal wind stress is generally strengthened at the LGM (Fig. 6). In addition to local increase, the wind stress is further enhanced by southward shift of maximum stress in the North Atlantic (Fig. 6c) and in the Southern Ocean (Fig. 6a). In contrast to the small changes in the Indo-Pacific Ocean, the wind stress in the North Atlantic Ocean shows an increase of over 0.05 N·m^{-2} near 30–60°N (Fig. 6c) mainly due to the southward shift of the core of westerlies. In the Southern Ocean, the stress is increased about 25% with a 3–4° poleward shift of maximum stress (Fig. 6a). These changes in surface wind stress have a significant impact on surface ocean circulation (see Sect. 4.2.1).

4.1.3 Comparisons with paleodata

The simulated SST differences (C-LGM-C-CTL and C-LGHG-C-CTL) are compared with four data-based reconstructions: the grided (2° × 2°) CLIMAP SSTs (CLIMAP project members 1981) based on the transfer function method with planktonic foraminiferal

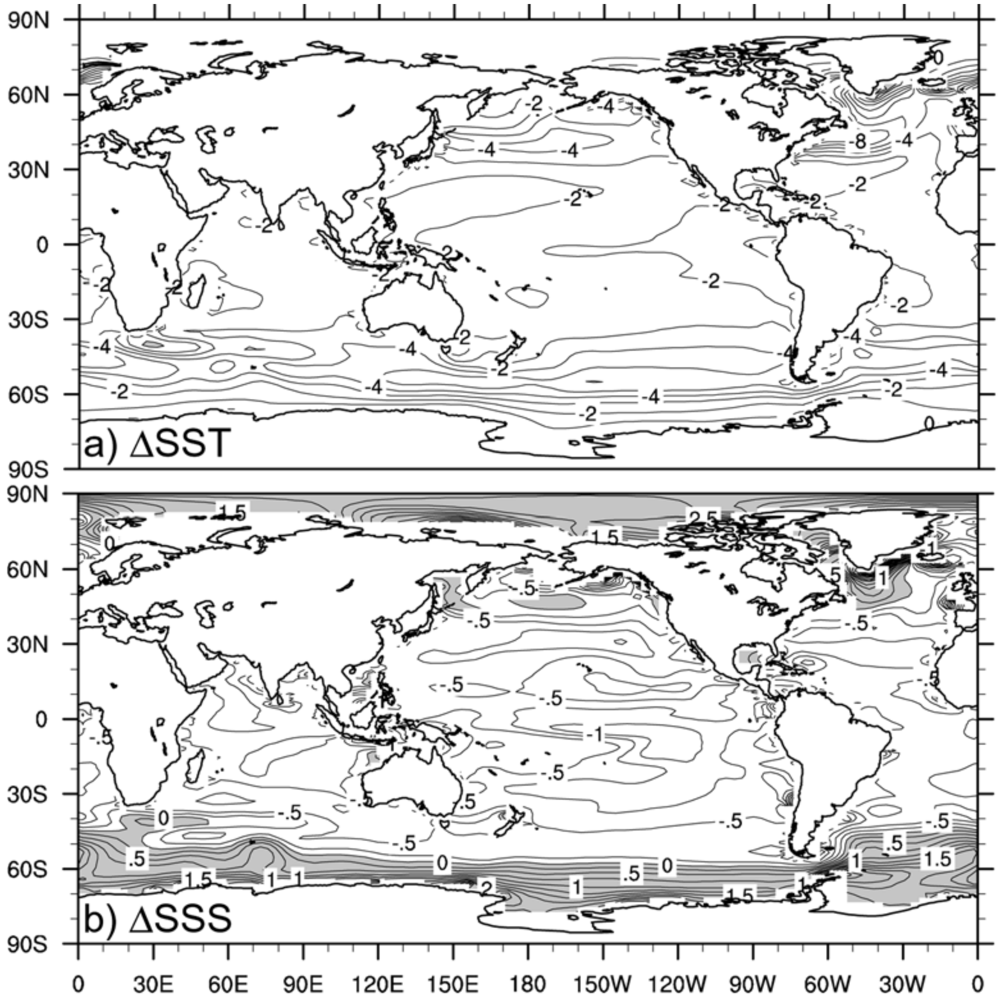

Fig. 5 Spatial patterns of annual glacial-modern differences of **a** SST (°C) and **b** SSS (psu). Contour intervals are 1 °C and 0.25 psu for **a** and **b** respectively. The positive values are *gray-shaded*

assemblages, the TEMPUS data set (Rosell-Melé et al. 1998) based on alkenones, the BLGM data set (Trend-Staid 1999) based on the modern analogue method with planktonic foraminiferal assemblages, and reconstructions based on dinocyst assemblages (de Vernal et al. 2000). The locations where these data were collected are shown in Fig. 7.

Generally speaking, the standard error of SST estimations based on planktonic foraminiferal assemblages is ± 1.5 °C for summer and ± 1.9 °C for winter (Moore et al. 1980). The alkenone-based reconstructions are associated with a standard error of ± 1.5 °C (Müller et al. 1998). The assessments using dinocyst assemblages are assigned standard errors of ± 1.6 °C and ± 1.2 °C for summer and winter respectively (de Vernal et al. 2000). An error range for the modern analogue technique can be estimated from the range of "*closest analogues*" identified. For a dissimilarity cutoff of 0.25, the range is typically about ± 5 °C (Fig 12 of Trend-Staid 1999).

The comparisons with CLIMAP estimates indicate two major features: (1) the absence of subtropical warming in the simulation, and (2) the simulation of conditions warmer than shown by CLIMAP in some regions of the northern midlatitude ocean (Fig. 8). The warm SST anomalies shown by CLIMAP estimates in the subtropical Pacific are replaced by 2–2.5 °C cooling in the coupled simulations. This simulated cooling is consistent, however, with temperature reconstructions using δ^{18}O in the subtropical North Pacific (Lee and Slowey 1999) and with alkenone-based SST reconstructions from the subtropics (Rosell-Melé et al. 1998). The simulation that conditions warmer than shown by CLIMAP estimates in the northern midlatitudes is consistent with dinocyst-based SST reconstructions from the North Atlantic (de Vernal et al. 2000).

In the tropics, the simulation is broadly consistent with alkenone data. In the high-latitude northern oceans, near 50°N, the simulations underestimate the cooling shown by the foraminiferal data sets, but are broadly in agreement with the reconstruction of smaller cooling based on the dinoflagellate data. There are also robust east–west features of the tropical SST anomaly, shown by alkenones as well as foraminifera. These features are not captured in our simulation.

Reconstructions of SSS at the LGM are only available for the northern North Atlantic Ocean (Duplessy et al. 1991; de Vernal et al. 2000). The simulated salinity

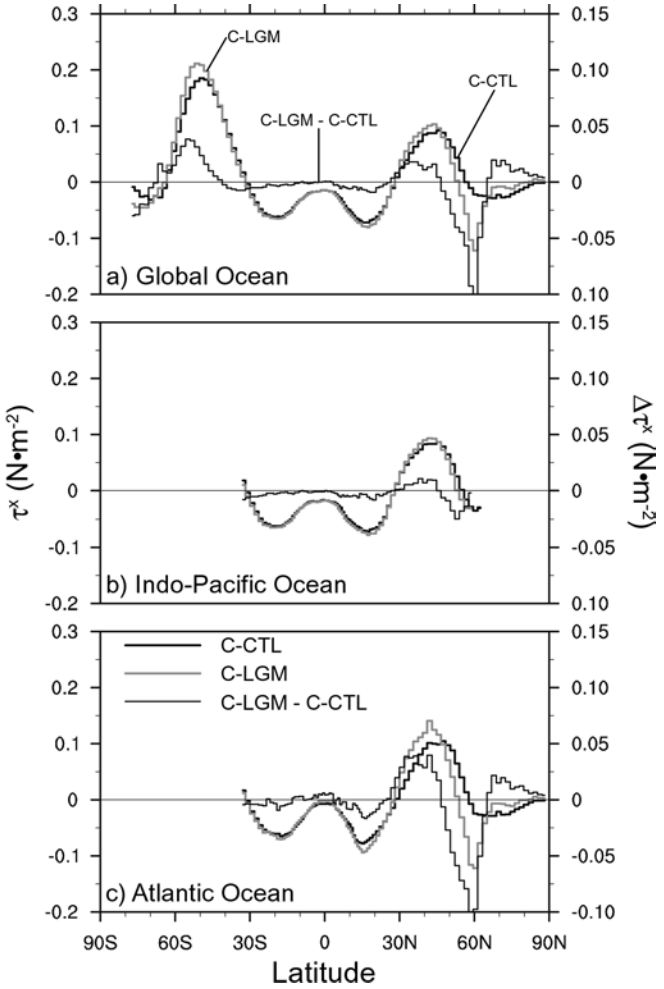

Fig. 6 The annual zonally averaged zonal wind stress (N·m^{-2}) for the control (C-CTL, *thick black line*), LGM (C-LGM, *thick gray line*) and the difference, LGM minus control (C-LGM-C-CTL, *thin black line*) in the **a** global Ocean, **b** Indo-Pacific Ocean, and **c** Atlantic Ocean including the Arctic. The control and the LGM wind stress scales are given on the *left-hand side* of figures. The anomalous wind stress (LGM minus control) scale is given on the *right-hand side* of figures. The *positive sign* indicates westerlies

changes at the LGM (Fig. 5b) are consistent with δ^{18}O-based reconstructions (Duplessy et al. 1991) showing that the largest freshening occurs in the Nordic Sea, where NADW is formed at present. However, SSS estimates based on dinocyst assemblages (de Vernal et al. 2000) indicate fresher conditions along the east coast of North America and on the margin of the Fennoscandian Ice-Sheet than shown either by the δ^{18}O reconstructions or in our simulation. These discrepancies probably reflect the importance of correctly incorporating the impact of sea-ice on salinity, both in making SSS reconstructions and in the simulations.

4.2 Ocean circulation

4.2.1 Wind-driven circulation

The ocean circulation at the LGM is changed in many respects relative to the modern situation. Both the transports of the Gulf Stream and the Kuroshio are enhanced (Fig. 9b) because of the overall increase of surface wind, thereby wind stress curl, in the subtropical oceans (see Fig. 6a). The Gulf Stream transport is enhanced by up to 10 Sv (~30% above modern strength) with a southward shift of its flow path (Fig. 9b) due to the strengthened and southward shift of westerlies in the North Atlantic (see Fig. 6c). The Kuroshio transport is also slightly enhanced at the LGM, ~4 Sv.

There is very little evidence which can be used to evaluate the simulated changes in wind-driven (surface) circulation patterns at the LGM. Although density contrasts inferred from δ^{18}O imply a reduction in transport through the Florida Straits (Lynch-Stieglitz et al. 1999), both paleonutrient measurements and inferred ventilation rates based on δ^{13}C and δ^{18}O measurements (Slowey and Curry 1992) suggest that the subtropical gyre in the North Atlantic was strengthened at the LGM. This is in good agreement with the

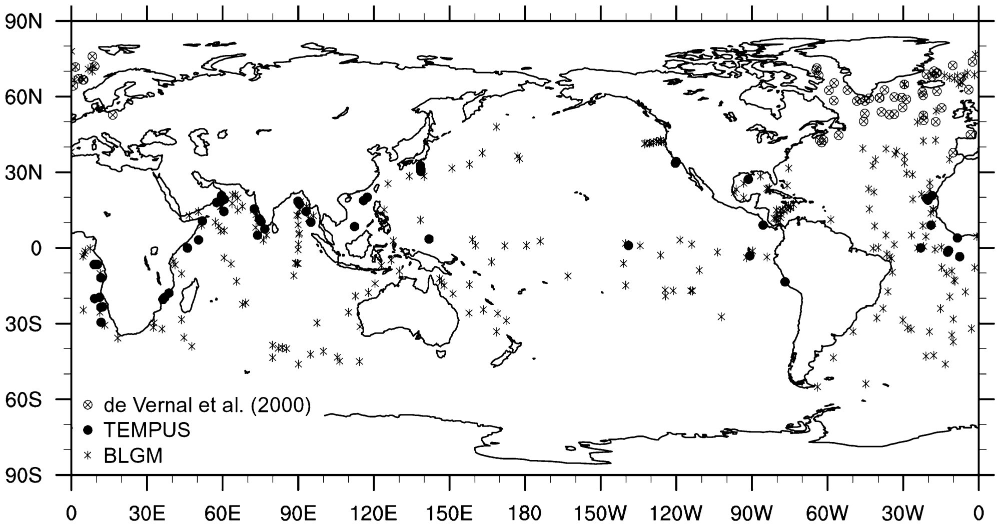

Fig. 7 The sites of SST estimations in the ocean

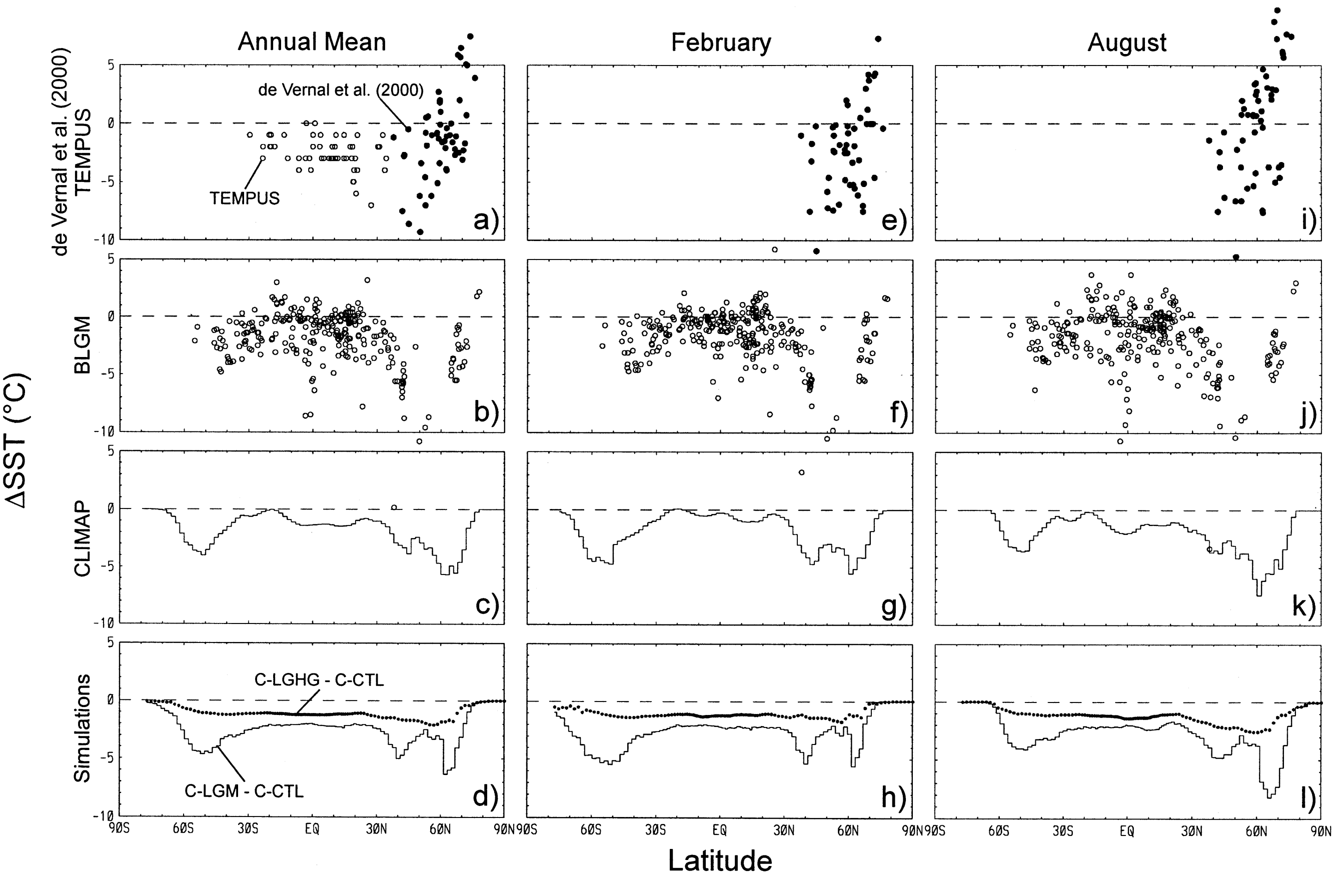

Fig. 8 The glacial-modern changes in zonally averaged annual SST (°C) from **a** TEMPUS (*open circle*) and dinocyst assemblages (*closed circle*), **b** BLGM (*open circle*), **c** CLIMAP (*line*) and **d** the simulations (*line and dots* represent LGM minus control, C-LGM-C-CTL, and LGM greenhouse gas forcing minus control, C-LGHG-C-CTL, respectively). **e**–**h** and **i**–**l** are the same as **a**–**d**, but for February and August respectively

simulated strengthening of the Gulf Stream (about 30% greater than modern, an increase that is statistically significant at the 95% level; Fig. 9b). On the basis of latitudinal variations between surface temperatures and the seasonal thermocline, it has been suggested that the Kuroshio was slightly enhanced at the LGM than today (Sawada and Handa 1998). The simulated Kuroshio is about 4 Sv stronger at the LGM than the modern, again in agreement with paleoceanographic data.

The transport of the ACC increased over 50% (~60 Sv) at the LGM compared to modern (Fig. 9b), primarily because of both the enhanced strength and the southward shift of maximum wind stress (see Fig. 6a). This southward shift appears to be due, at least in part, to enhanced low-level baroclinicity and stronger low-level wind at the LGM sea-ice front. In the Southern Ocean, the zonal wind stress is increased about 25% with a 3–4° poleward shift of maximum stress (see Fig. 6a). Klinck and Smith (1993) show that both the strength and the position of wind stress are closely tied to the transport of the ACC; the transport of the ACC increases linearly with zonal wind stress and diminished blocking effect by the South American Continent. The strength of ACC is also affected by the strength of the thernohaline circulation off the Antarctic shelf. The sensitivity experiments using NCOM, the same ocean model as present study, show that the strength of ACC increases with meridional overturning strength off the Antarctic shelf (Gent et al. 2001). The LGM meridional overturning circulation in the Antarctic Ocean enhanced by 2 Sv (Fig. 10a, d). This enhanced overturning circulation also contributes to the ACC increase at the LGM. In C-CTL, the maximum transport of the ACC (120 Sv) occurs in the Drake Passage, which is consistent with hydrographic data (Whitworth 1983).

The various throughflows at the LGM and the modern are diagnosed using the island circulation rule (Godfrey 1989), equivalent to a maximum transport through straits (Table 4). The Indonesian throughflow during the LGM decreased by 20% (~5 Sv). The circulation through the Tasman Sea increased by 100% (~14 Sv) and the Agulhas current decreased about 7 Sv. Enhanced palaeoproductivity in the Timor Straits (Müller and Opdyke 2000) implies decreased Indonesian throughflow during the LGM, consistent with the simulated decrease.

Fig. 9 The annual oceanic barotropic stream function (Sv = 10^6 m^3·s) of the **a** control (C-CTL) and the difference, **b** LGM minus control (C-LGM-C-CTL). Contour intervals are 20 Sv and 10 Sv for **a** and **b** respectively. Negative values are *dashed* and *gray-shaded*

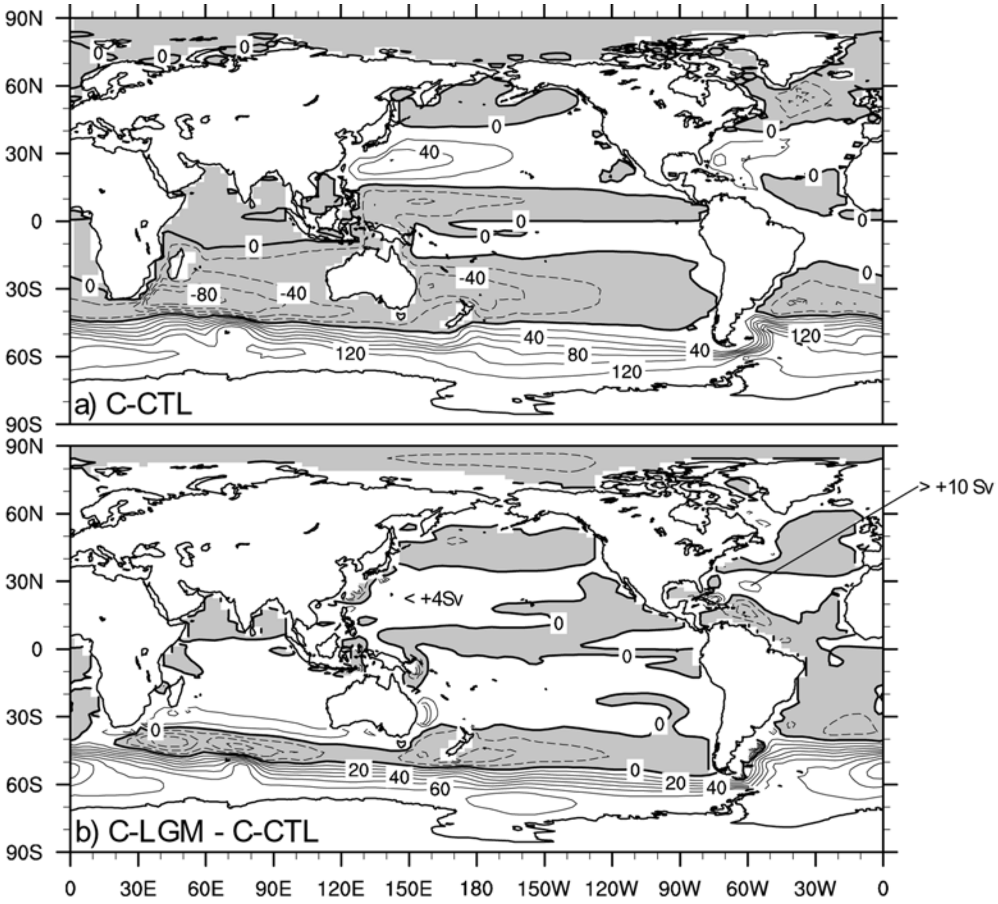

4.2.2 Thermohaline circulation

Due to the substantial changes of SST and SSS (the surface buoyancy forcing), the oceanic overturning circulation is in a different mode of operation at the LGM (Broecker et al. 1985; Broecker and Denton 1989). Although the coupled models (C-CTL and C-LGM) are integrated for only 110 years, they started from more glacial-like ocean state than the modern control because of a deep-ocean acceleration used during ocean spin-up. Although small changes in the thermohaline circulation are still occurring (see Fig. 24b) the general tendency is clear. Furthermore, an LGM simulation started from modern ocean state (same initial state of C-CTL ocean) integrated for 300 surface model years using a deep-ocean acceleration, which is equivalent to 15,000 years in the deep-ocean, shows the same final overturning circulation patterns and strength as in the present study (see Fig. 24b).

There is a weakened meridional overturning circulation at the LGM compared to the modern control as suggested by paleoceanographic data (Duplessy et al. 1988; Broecker and Denton 1989; Lea and Boyle 1990). In the region of deep-water formation in the Northern Hemisphere (Fig. 10a, d) the flow is 30 Sv in C-CTL and 24 Sv in C-LGM. The same tendency appears in the North Atlantic, 30 Sv in C-CTL and 24 Sv in C-LGM (Fig. 10c, f). Furthermore, both the global and the North Atlantic overturning cells are significantly shallower in the LGM simulation than in the modern control. The simulated glacial overturning cell in the North Atlantic shallower by about 1000–2000 m than the modern, and is accompanied by an enhanced intrusion of bottom water from the Southern Ocean into the North Atlantic, which is consistent with paleoceanographic evidences (Duplessy et al. 1988; Broecker and Denton 1989; Lea and Boyle 1990).

The deep-water formation site can be traced by using the oceanic mixed-layer depth. In this study, we use a definition of the oceanic mixed-layer depth of Large et al. (1997). The formation site of the NADW at the LGM, as indicated by the deep oceanic mixed-layer depth, migrates from the Labrador Sea, south of Iceland and the Nordic Seas at modern control (Fig. 11a) to mainly south of Greenland at the LGM (Fig. 11b). As inferred from the paleoceanographic data, deep-water also forms in the seasonally ice-free Nordic Seas at the LGM (Weinelt et al. 1996; Rosell-Melé and Koc 1997). The remarkable enhancement of the deep-water formation in the Weddell Sea at the LGM is also apparent in the oceanic mixed-layer depth analysis (Fig. 11c, d).

Since the surface density anomaly, a combination of the thermal and the haline density anomalies, can produce thermohaline circulation change, we diagnose the surface density flux (kg·m^{-2}·s^{-1}) (Schmitt et al. 1989; Speer and Tziperman 1992; Doney et al. 1998). The

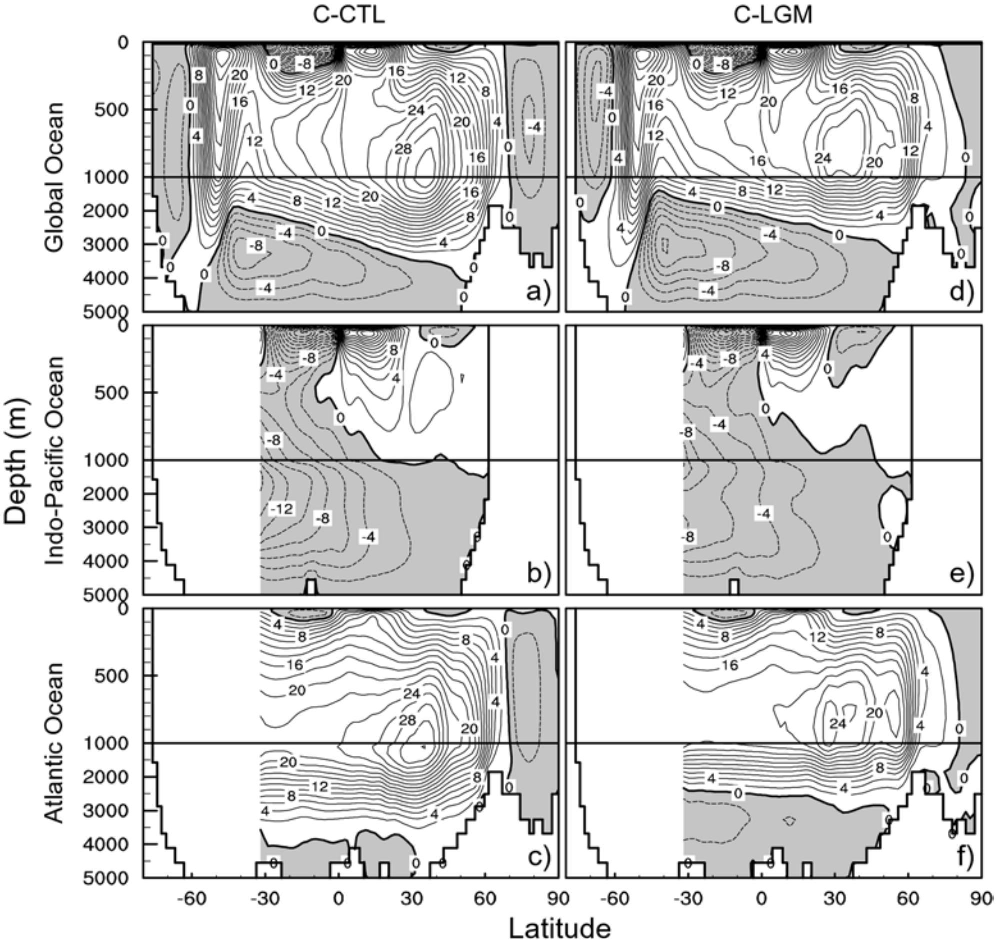

Fig. 10 The annual meridional overturning stream function (Sv) in the **a** global Ocean, **b** Indo-Pacific Ocean and **c** Atlantic Ocean including the Arctic of the modern control (C-CTL); **d–f** are the same as **a–c** but for the simulation of the LGM (C-LGM). Contour interval is 2 Sv. Negative values are *dashed* and *gray-shaded*

Table 4 The strength of the various throughflows (Sv) in the ocean at the modern and at the LGM. The numbers in parentheses epresent the ±1 standard deviation over the last 50 years in the simulations

	C-CTL	C-LGM
Indonesian Throughflow	26.1(1.5)	19.7(0.9)
Tasman Sea	12.3(3.3)	26.9(3.7)
Mozambique Channel (Agulhas current)	34.9(1.4)	28.2(1.3)

density flux is divided into thermal and haline density flux components to evaluate the relative contribution of two surface buoyancy forces on the LGM thermohaline circulation change. The surface density flux is defined as,

$$F_\rho = -\alpha F_T + \beta F_S = -\alpha \cdot \frac{Q}{C_p} + \beta \cdot \rho(0,T) \cdot \frac{(E-P-I)\cdot S}{1-S} \ , \qquad (1)$$

with the thermal expansion ($\alpha = -\frac{1}{\rho}\frac{\partial \rho}{\partial T}|_{p,S}$) and haline contraction coefficients ($\beta = \frac{1}{\rho}\frac{\partial \rho}{\partial S}|_{p,T}$).

In these expressions, C_p, $\rho(S, T)$, p, T and S are specific heat, density, pressure, sea surface temperature and sea surface salinity respectively. Q, E, P and I represent net heat flux, evaporation, precipitation, and water flux by sea-ice melting and growth respectively.

Figure 12 shows the surface density flux changes at the LGM. While the thermal density flux change dominates in the North Atlantic, the haline density flux change dominates in the Southern Ocean. As in the modern climate, the NADW formation rate at the LGM is primarily controlled by the thermal density flux, i.e., the export of cold air from the North American continent. Although the haline density flux is also increased at the LGM mainly in the Nordic Seas, an intense surface cooling over 8 °C (see Fig. 5a) makes the surface waters dense enough to form the NADW in the south of Greenland at the LGM. The density flux change in the North Atlantic, however, does not indicate a reduced NADW formation at the LGM, but rather indicates a migration of deep-water formation site. On the contrary, the Southern Ocean shows a significant increase of density flux at the LGM (Fig. 12f). Furthermore, this density flux change in the Southern Ocean is attributable to the haline density flux change under the regions of year round sea-ice cover at the LGM (Figs. 12d, 20). The water formation rate diagnosed by only using the surface density flux in the North Atlantic shows similar NADW formation rate, but significant increase of AABW formation rate in the Southern Ocean by

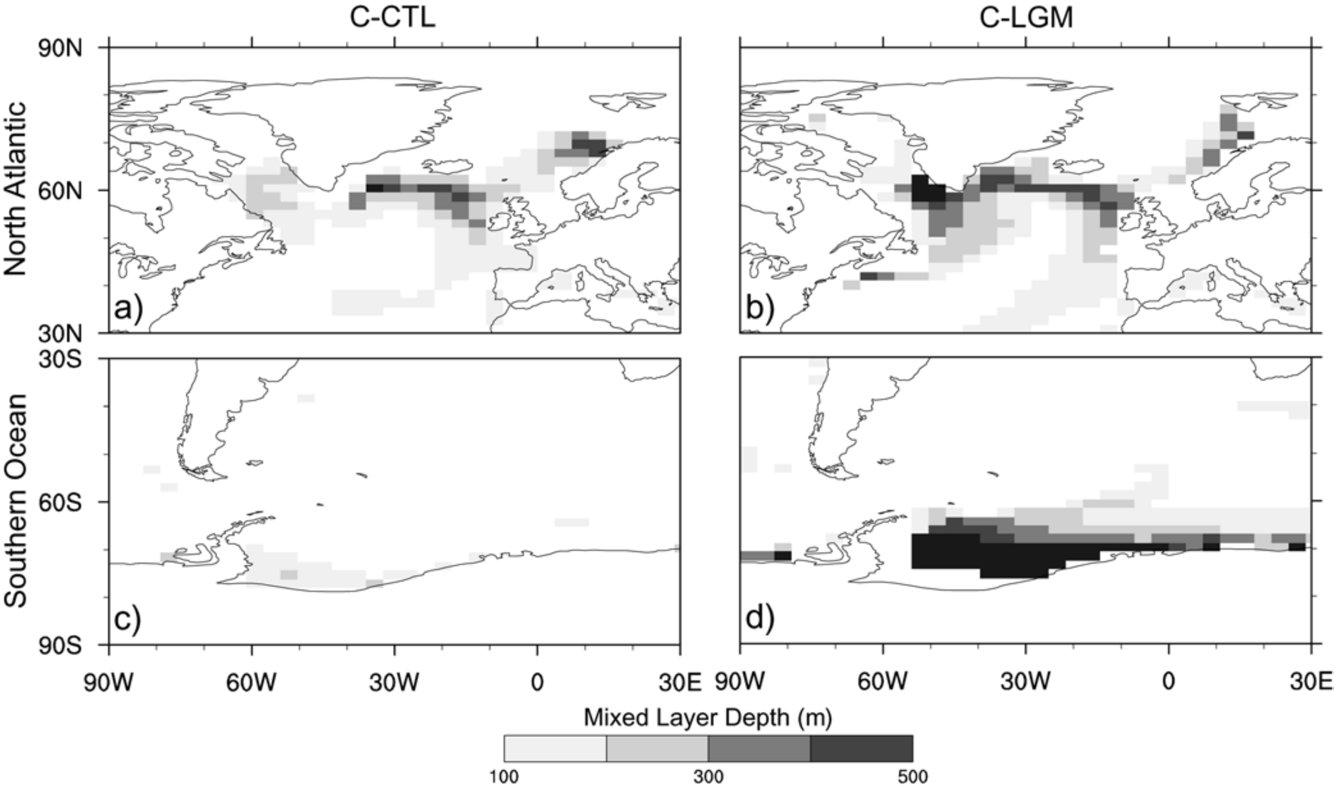

Fig. 11 The annual oceanic mixed-layer depth of the **a** modern control (C-CTL) and **b** LGM (C-LGM) in the North Atlantic; **c**, **d** are the same as **a**, **b** but for the Southern Ocean

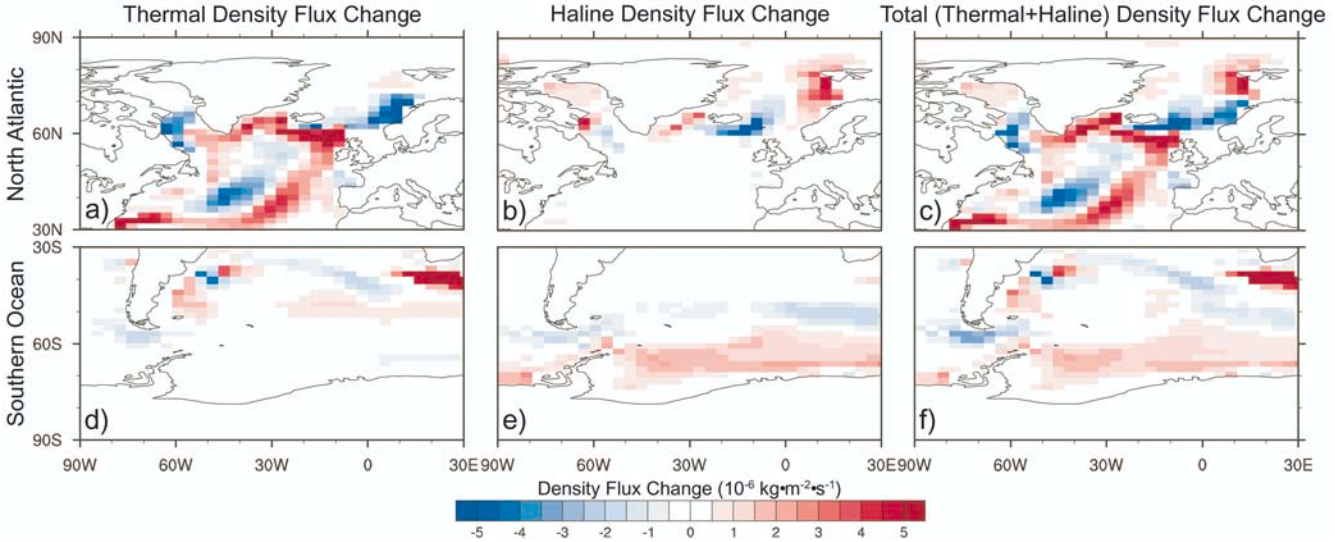

Fig. 12 The annual glacial-modern change in **a** thermal density flux, **b** haline density flux, and **c** total (thermal plus haline) density flux in the North Atlantic; **d**–**f** are the same as **a**–**c** but for the Southern Ocean

enhanced salt pump (Broecker and Peng 1987) at the LGM compared to the modern (Shin 2002). It implies that the enhanced AABW formation by sea-ice change controls the depth and strength of NADW at the LGM. A more complete analysis on the cause of LGM thermohaline circulation will be presented elsewhere.

4.3 Atmospheric circulation

4.3.1 Surface circulation

The maximum surface cooling (about 20 °C) occurs in the high latitudes of the Northern and the Southern

Hemispheres during winter because of the presence of ice-sheets and expanded sea-ice (Fig. 13). The average cooling over land in the tropics is 3 °C (Fig. 13) and is spatially rather uniform (Fig. 14). Greenhouse gases explain only half of the glacial-age temperature change in the tropics. As discussed in Sect. 4.1.1, the positive water-vapor feedback also contributes to the simulated tropical cooling at the LGM.

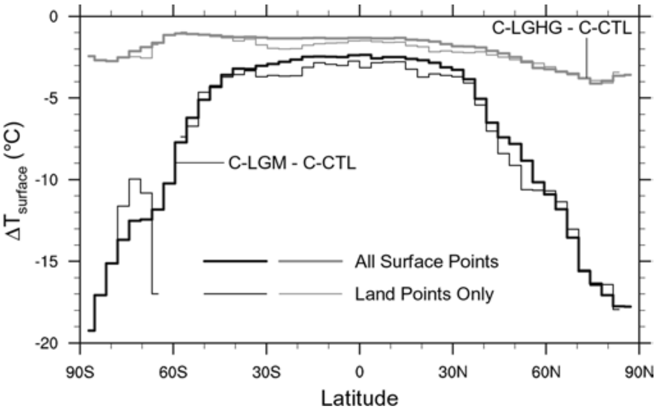

Fig. 13 The zonally averaged annual surface temperature differences (°C) for the LGM minus control (C-LGM-C-CTL, *black line*) and for the LGM greenhouse gas forcing minus control (C-LGHG-C-CTL, *gray line*). The *thick* and *thin lines* represent the differences computed over all surface points and land points only respectively

The changes of precipitation at the LGM are mainly concentrated near the Intertropical Convergence Zone (ITCZ) with a maximum decrease of over 200 cm·year^{-1} (≥50%) in the Pacific Ocean (Fig. 15). The precipitation in monsoon regions is also significantly decreased, e.g., in India, North Africa, southwest US/Mexico and southeastern China (Fig. 15d). Increased precipitation occurs over the subtropical ocean (20°–30°) of the winter hemisphere due to the enhanced subtropical to midlatitude storms at the LGM (Fig. 15b, d). The precipitation is increased over the eastern portion of the North Atlantic Ocean between 30–50°N due to the well-developed anomalous cyclonic circulation during winter (Fig. 16b).

The reduced monsoon strength during the LGM is also apparent in the 850 hPa wind difference between C-CTL and C-LGM during boreal summer (Fig. 16d). The surface wind in the Arabian Sea, supplying the major moisture source of monsoon rainfall to India, is reduced due to reduced land-ocean temperature contrast. This reduction of the low-level Arabian Sea wind

Fig. 14 LGM changes (C-LGM-C-CTL) of surface temperature (°C) during the Northern Hemisphere **a** winter (DJF) and **b** summer (JJA). Contour interval is 2 °C

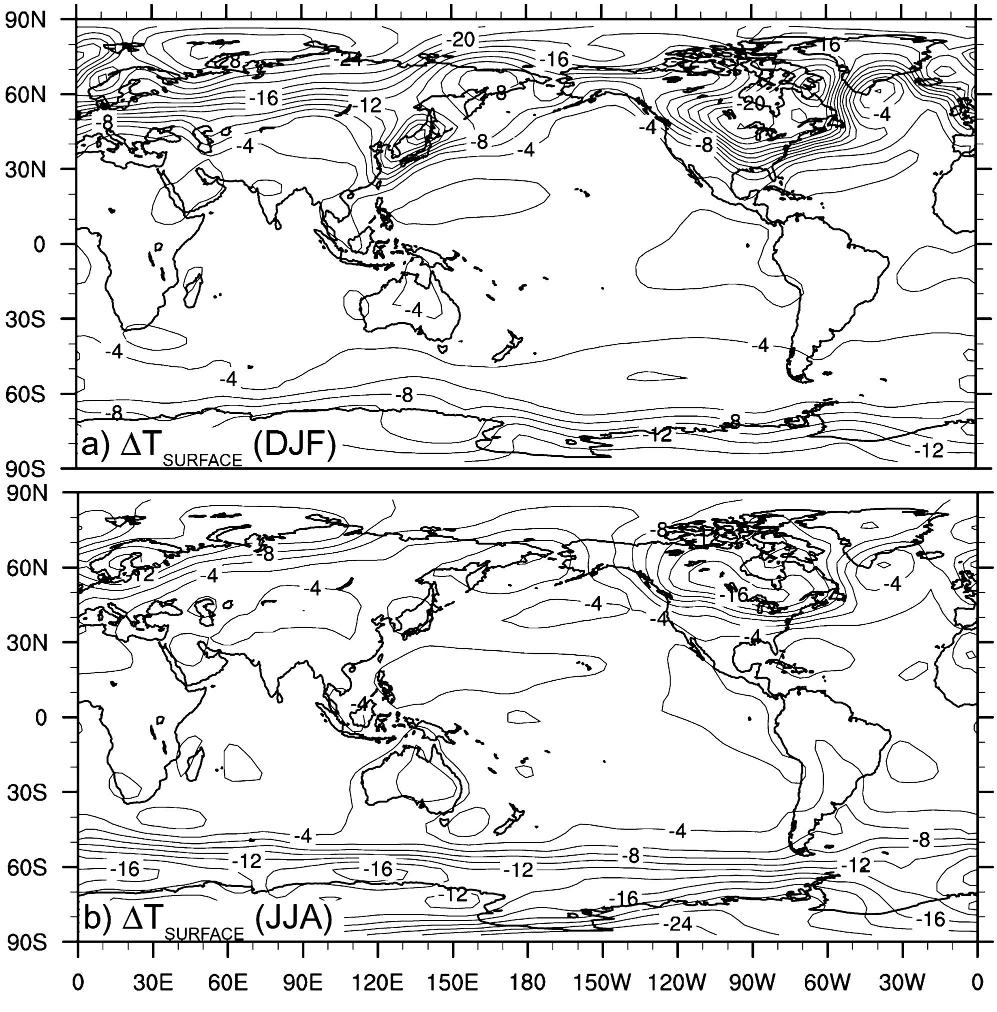

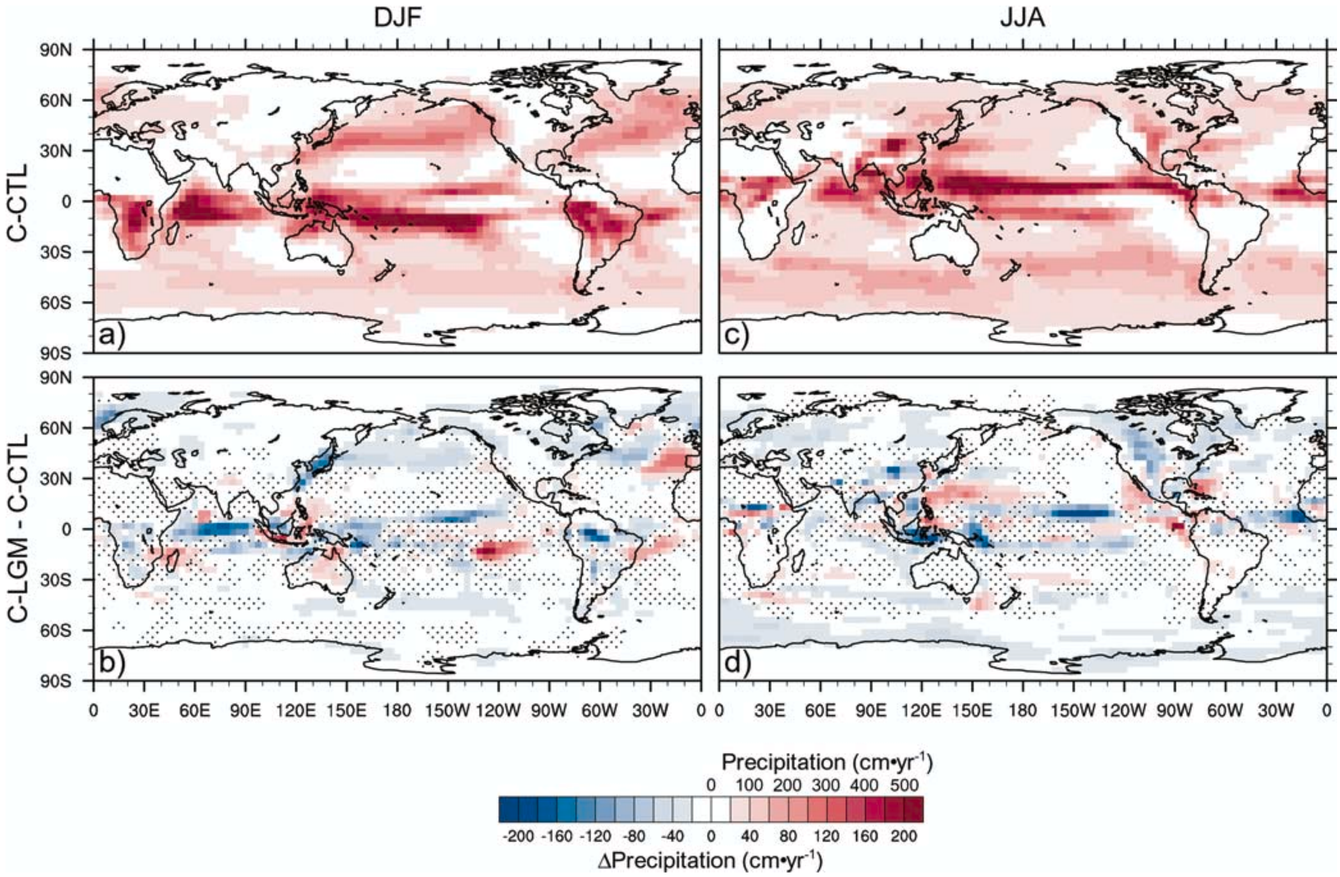

Fig. 15 The precipitation (cm·yr^{-1}) of the **a** control (C-CTL) and **b** difference between LGM and control (C-LGM-C-CTL) during the Northern Hemisphere winter (DJF); **c**, **d** show the same variables as **a**, **b**, but for the Northern Hemisphere summer (JJA). Regions where statistical significance is less than 95% are **dotted** in **b** and **d**

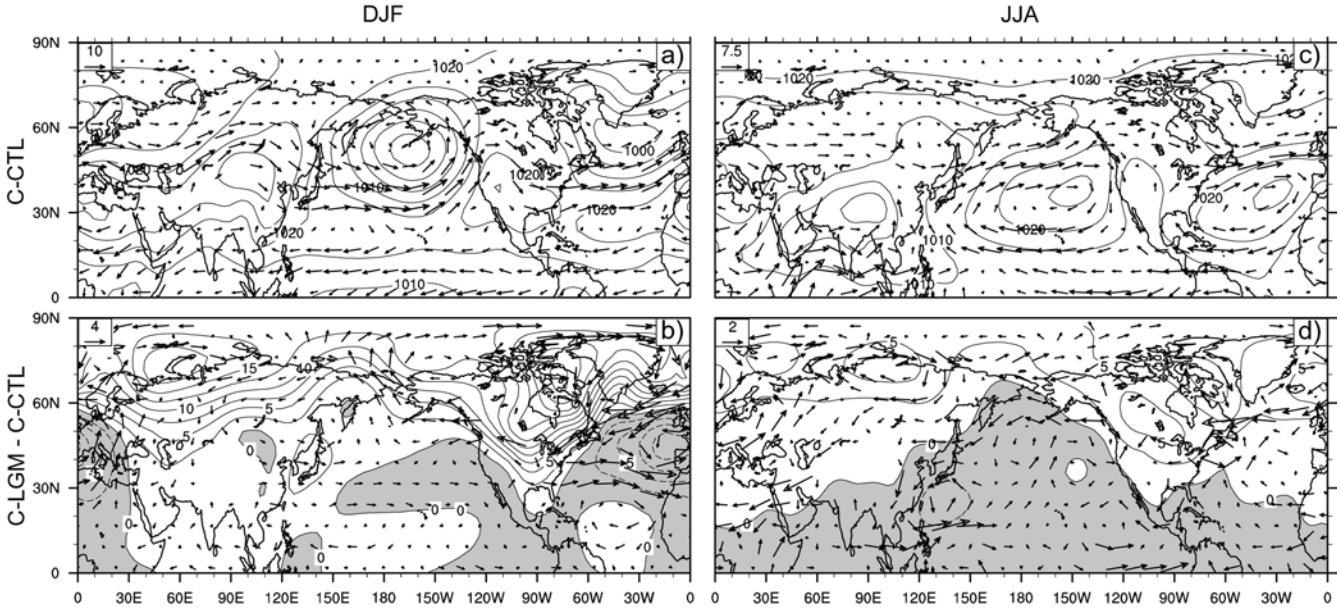

Fig. 16 The maps of the 850 hPa wind velocity (m·s^{-1}) and the surface pressure (hPa) in the Northern Hemisphere of the **a** control (C-CTL) and difference, **b** LGM minus control (C-LGM-C-CTL), during the Northern Hemisphere winter (DJF); **c**, **d** are the same as **a**, **b**, but for the Northern Hemisphere summer (JJA). The reference *wind vectors* are shown in the *upper left corner* of each map. Contour intervals are 5 hPa in **a** and **c**, 2.5 hPa in **b** and **d**. Negative values in **b** and **d** are *dashed* and *gray-shaded*

during the summer monsoon is less than shown in earlier simulations with prescribed CLIMAP SSTs (e.g., COHMAP Members 1988).

A well-developed anticyclonic circulation is evident in the vicinity of ice-sheets during boreal winter due to the cooling and associated divergent outflow (Fig. 16b). In comparison with earlier simulations with prescribed CLIMAP SSTs (e.g., COHMAP Members 1988) where the wintertime Aleutian Low was greatly deepened, our simulation shows a small increase. In conjunction with the southward-shifted westerlies in the North Atlantic, a very strong cyclonic circulation develops in the midlatitude eastern North Atlantic Ocean during winter. This enhanced westerly flow advects a warm maritime air mass into the western European continent.

In the tropics of the Northern Hemisphere, the trade winds are strengthened in both winter and summer season in the Atlantic and weakened in the Pacific basin. The enhanced trade wind during the glacial period over the North Atlantic is consistent with the paleowind reconstructions inferred from dust deposits (Sarnthein et al. 1981) and the grain size distribution of eolian sediments (Rea 1994). On the contrary, the decrease in trade wind in the Pacific Ocean seems to contradict the eolian sediment analysis (Janecek and Rea 1985; Rea 1994) and the oceanic thermocline changes (Andreasen and Ravelo 1997; Trend-Staid 1999; Liu et al. 2000).

4.3.2 Zonally averaged circulation

The seasonally reversing cross-equatorial flow associated with the Hadley circulation during the LGM is increased over 10% compared to the C-CTL (Fig. 17d, e). In the C-CTL, the maximum overturning strength is 220 × 10^9 and 200 × 10^9 kg·s^{-1} during boreal winter and summer respectively (Fig. 17a, b), which agrees well with climatological calculations (Peixoto and Oort 1992). In conjunction with the small change of SST gradient in the tropics (Fig. 8h, i), the seasonal increase of the Hadley cell can be attributed to increased meridional SST gradient in the midlatitudes as noticed in a coupled model by Bush and Philander (1999). The annual mean Hadley circulation, however, remains little changed (Fig. 17f).

The zonally averaged vertical atmospheric structures, temperature and specific humidity (Fig. 18) indicate that tropospheric cooling extends beyond 200 hPa in the tropics with a maximum cooling of 5 °C in the upper troposphere (Fig. 18b). Baroclinicity is increased in the mid-troposphere during the LGM. The cooling anomaly of 4 ~ 5 °C in the tropics is increased meridionally up to 16 °C at both poles. The atmospheric moisture content (specific humidity) is reduced in the entire atmospheric column with a maximum reduction in the lower troposphere (Fig. 18d). This indicates that not only are conditions colder and drier during the glacial-age, but also that positive water-vapor feedback enhances the cooling (Broecker 1995; see Sect. 4.1.1).

4.4 Meridional heat transport

Changes in the atmospheric and oceanic circulations have resulted in changes of meridional heat transport in the coupled simulations. The total heat transport of the

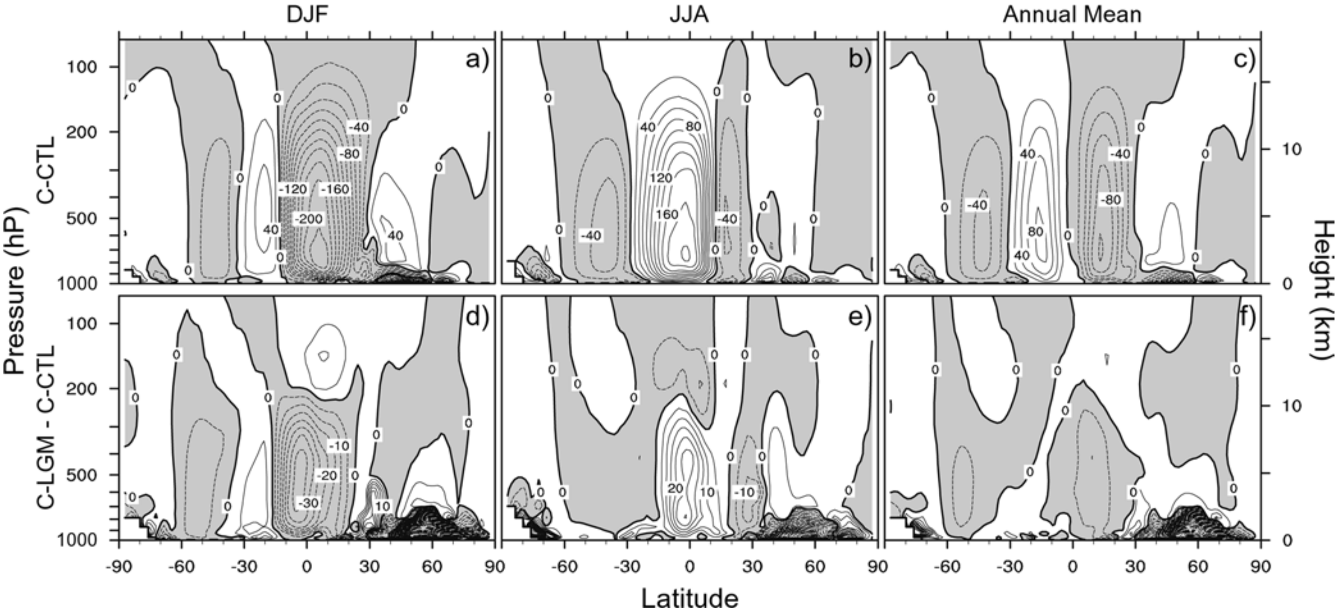

Fig. 17 The atmospheric meridional overturning circulation (10^9 kg·s^{-1}) during the **a** Northern Hemispheric winter (DJF), **b** Northern Hemispheric summer (JJA), and **c** annual mean of the modern control (C-CTL). Contour intervals are 20 × 10^9 kg·s^{-1}; **d**–**f** are the same as **a**–**c**, but for the difference, LGM minus control (C-LGM-C-CTL. Contour interval is 5 × 10^9 kg·s^{-1}). Negative values are *dashed* and *gray-shaded*

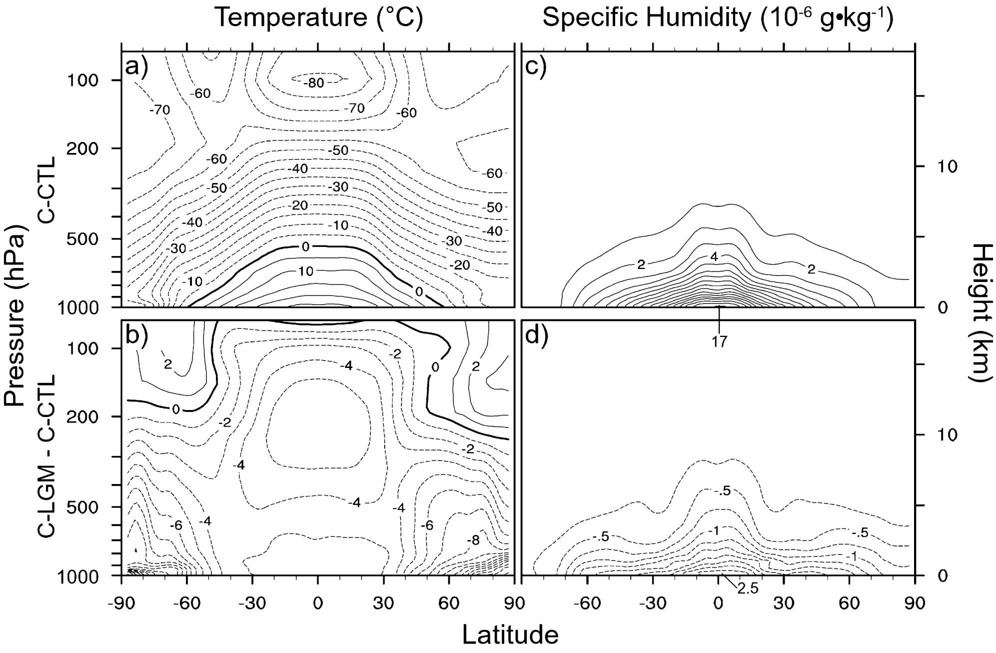

Fig. 18 The zonally averaged annual air temperature (°C) for the **a** control (C-CTL. Contour interval is 5 °C) and difference, **b** LGM minus control (C-LGM-C-CTL. Contour interval is 1 °C); **c**, **d** are the same as **a**, **b**, but for the specific humidity (10^{-6} g·kg^{-1}). Contour interval is 1×10^{-6} g·kg^{-1} for **c**. For **d**, contour interval is 0.25×10^{-6} g·kg^{-1}

atmosphere-ocean system in each latitudinal band is diagnosed from the difference between the net solar flux and outgoing long wave radiative flux at the top-of-the-atmosphere,

$$\mathbf{T}_{\mathrm{TOTAL}} = \mathbf{T}_{\mathrm{ATM}} + \mathbf{T}_{\mathrm{OCN}} = 2\pi a^2 \times \int_{-\pi/2}^{\varphi} (\mathbf{S}_{\mathrm{TOA}} - \mathbf{L}_{\mathrm{TOA}}) \cdot \cos\varphi \cdot \mathrm{d}\varphi \ , \qquad (2)$$

where, $\mathbf{T}_{\mathrm{TOTAL}}$, $\mathbf{T}_{\mathrm{ATM}}$, and $\mathbf{T}_{\mathrm{OCN}}$ are the total, atmospheric, and oceanic heat transport respectively, a is radius of the Earth, φ is latitude starting from South Pole, $\mathbf{S}_{\mathrm{TOA}}$ is net solar flux at the top of the atmosphere, and $\mathbf{L}_{\mathrm{TOA}}$ is outgoing long wave radiative flux at the top-of-the-atmosphere. Any imbalance of energy in Eq. (2) is removed by a constant correction applied uniformly over the globe.

The oceanic heat transport in each latitudinal circle, $\mathbf{T}_{\mathrm{OCN}}$, is calculated by zonal and vertical integration of the meridional temperature flux, i.e.,

$$\mathbf{T}_{\mathrm{OCN}} = \rho c_0 a \int\int \mathbf{vT} \cdot \cos\varphi \cdot \mathrm{d}\lambda \cdot \mathrm{d}z \ , \qquad (3)$$

where, $\mathbf{T}_{\mathrm{OCN}}$ is the oceanic heat transport, ρ is the density of the ocean water (1000 kg·m^{-3}), c_0 is the specific heat of the ocean water (4187 J·kg^{-1}·K^{-1}), λ is longitude, $\mathbf{v}$ is the north–south component of the ocean current, and $\mathbf{T}$ is the ocean temperature. The atmospheric heat transport, $\mathbf{T}_{\mathrm{ATM}}$, can be diagnosed as a residual, $\mathbf{T}_{\mathrm{TOTAL}} - \mathbf{T}_{\mathrm{OCN}}$.

The simulated atmospheric heat transport in C-CTL (Fig. 19a) is comparable to the calculations using climatological data (Peixoto and Oort 1992). The maximum atmospheric heat transport appears at 40° in both hemispheres with a maximum of 5 PW (PW = 10^{15} W). At the LGM, the atmospheric heat transport is increased in both hemispheres except in the tropics of the Southern Hemisphere (10–30°S; Fig. 19b). On the other hand, the atmospheric heat transport by the LGM greenhouse gas reduction is decreased in the Northern Hemisphere and increased in the Southern Hemisphere (Fig. 19c). This implies that the enhanced Northern Hemispheric atmospheric heat transport at the LGM is caused by the presence of large ice-sheets, very likely through the increased baroclinic eddy activity in the atmosphere.

Globally, the oceanic heat transport change at the LGM follows that of the Indo-Pacific Ocean except in the northern midlatitudes where the oceanic heat transport is increased mainly due to the increase in the North Atlantic by enhanced Gulf Stream (Fig. 19b). In the Southern Hemisphere, the heat transport of both C-LGM and C-LGHG are increased in the subtropics. In C-LGM, the increase is over 30%. Beyond 50°S, the strengthened ACC prohibits southward heat transport in LGM simulations. The heat transport is decreased in the Indo-Pacific Ocean and increased in the Atlantic Ocean at the LGM (Fig. 19b), which is the opposite partitioning of the oceanic heat transport to that shown both in earlier simulations (Ganopolski et al. 1998; Weaver et al. 1998) and C-LGHG (Fig. 19c). The causes of this difference may be related to differences in the change of strength of the meridional overturning circulation. Despite the differences in heat transport of individual ocean basins, the coupled experiments consistently show a change of maximum northward oceanic heat transport at the LGM (+30% in the Southern Hemisphere and –15% in the Northern Hemisphere in this simulation).

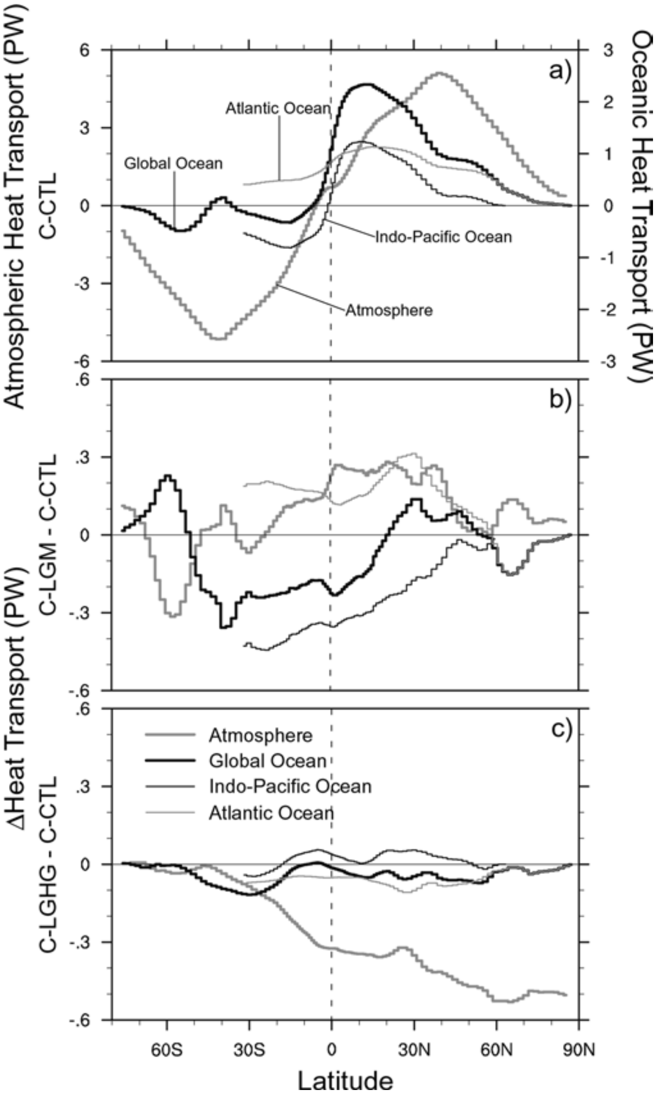

Fig. 19 The annual meridional heat transport (PW) for the **a** control (C-CTL), and differences, **b** LGM minus control (C-LGM-C-CTL) and **c** LGM greenhouse gas forcing minus control (C-LGHG-C-CTL). The *thick black* and *gray lines* represent the oceanic and atmospheric heat transport respectively. The *thin black* and *gray lines* represent the oceanic heat transport in the Indo-Pacific and in the Atlantic Ocean respectively

4.5 Sea-ice

Sea-ice cover changes significantly at the LGM. In C-LGM, the thin ice (≤ 1 m) in both the North Pacific and the North Atlantic expands farther southward compared to the modern. Thick (≥4 m) ice covers the entire Arctic during both winter and summer (Fig. 20e, g). However, the maximum sea-ice thickness during the austral winter in C-LGM is similar to C-CTL in the Southern Ocean. Thin ice advances 10° equatorward in the Atlantic and in the Pacific Ocean and 5° in the Indian Ocean during austral winter at the LGM compared to the modern control (C-CTL) (Fig. 20b, f). The seasonal fluctuation of the sea-ice margin in C-LGM is ca 10° larger than C-CTL in the Southern Ocean. This large movement of the sea-ice margin is not consistent with the CLIMAP reconstructions but is consistent with the recent reevaluation of sea-ice margin in the Southern Ocean (Crosta et al. 1998). The results may be influenced by biases in the control. For example, in C-CTL, the sea-ice cover in the North Pacific is overestimated compared to the observation during boreal winter (Fig. 20a).

There are continuing uncertainties about the seasonal extent of sea-ice in the North Atlantic at the LGM. Recent work (e.g., de Vernal et al. 2000) suggests the North Atlantic was more open, at least seasonally, than indicated by CLIMAP (1981). Figure 21 compares the number of months of sea-ice cover as depicted in the CLIMAP reconstruction and the simulation. In CLIMAP reconstructions, the fractional sea-ice cover is not estimated. Therefore, the sea-ice fraction in CLIMAP data is either 0% or 100%. Since the CSIM calculates the fractional sea-ice cover, the comparisons are performed for two cases: ice fraction larger than 0% and larger than 75%. When the months of sea-ice cover are calculated with a strict criterion, > 0%, the simulated sea-ice cover is overestimated compared to CLIMAP. But with a criterion of > 75%, much less monthly sea-ice cover results with the seasonal openings in the Norwegian Sea. The seasonal opening of sea-ice in the Norwegian Sea at the LGM is suggested by recent studies (Weinelt et al. 1996; Rosell-Melé and Koc 1997). But compared to the reconstructions based upon dinocyst assemblages (de Vernal et al. 2000), the simulated openings in the Nordic seas are less than the estimates suggested by paleodata.

5 Climate change over land surface: comparisons with paleodata

5.1 Tropics

The Farrera et al. (1999) data set provides quantitative estimates of the LGM changes in mean temperature of the coldest month (MTCO), based on records of vegetation changes, and mean annual surface temperature (MAT), based on noble gas paleothermometry and isotope measurements on speleothems, for the region between 32°N and 33°S. The changes in MTCO and MAT are broadly similar in the low latitudes because the low seasonality of insolation in the tropics offers little scope for seasonal changes in temperature. Both variables indicate that land temperatures in the tropics were on average 2.5 to 3 °C cooler than today at modern sea level. The simulated change in tropical temperatures over land (3 °C) is thus in good agreement with the data-based estimate. However, the data indicate that the magnitude of this cooling is not spatially uniform: Central America and northern South America cooled by 5–6 °C, regions peripheral to the Indian Ocean (southern and eastern Africa, India and Indonesia) cooled by 2–3 °C, and the low-elevation cooling in

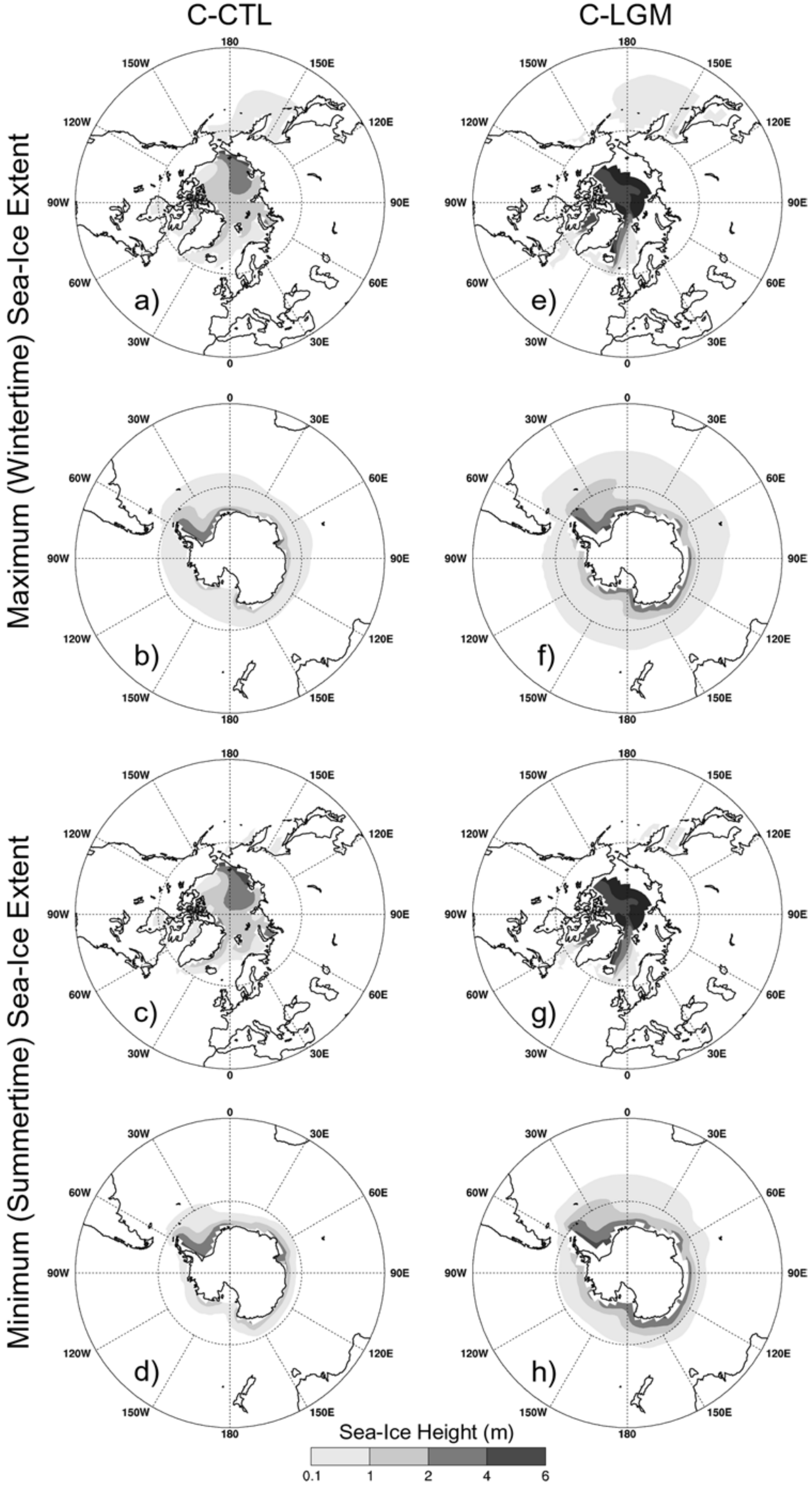

Fig. 20 Sea-ice thickness (m) in **a** February for the Northern Hemisphere, **b** August for the Southern Hemisphere, **c** August for the Northern Hemisphere and **d** February for the Southern Hemisphere of the control (C-CTL); **e**–**h** show the same variables as **a**–**d**, but for the LGM simulation (C-LGM)

Papua New Guinea and the islands of the western Pacific Ocean was no more than about 1–2 °C (Fig. 22). By contrast, the spatial structure of the tropical cooling in our simulations is relatively uniform. Also, the reconstructed change in MTCO at low-elevation sites in subtropical southeastern North America and southern China was substantially larger than simulated (Table 5).

The Farrera et al. (1999) data set also provides reconstructions of the changes in lapse rate at the LGM. The average change in lapse rate is –0.8 K·km^{-1}. The simulated change in lapse rate (–0.2 K·km^{-1}, figure not shown) is thus about 25% of the changes estimated from data. The data show the largest changes in lapse rate in the western Pacific Ocean (about –2 K·km^{-1}). The simulation, however, shows the largest steepening in the eastern Pacific Ocean and a shallowing of lapse rates in the western Pacific. Thus the spatial patterning shown by the simulation is not consistent with the observed spatial variations in lapse rate within the tropics.

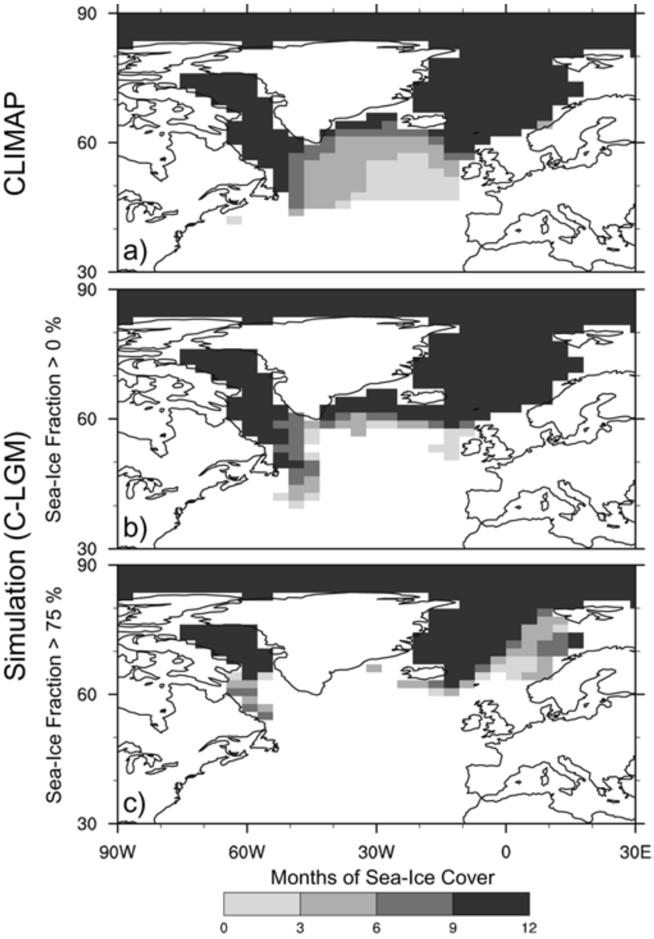

Fig. 21 The counts of monthly sea-ice cover in the North Atlantic from the **a** CLIMAP estimates, **b** LGM (C-LGM, sea-ice fraction > 0%) and **c** LGM (C-LGM, sea-ice fraction > 75%)

Paleo-environmental data, including vegetation-based estimates of plant-available moisture (PAM) (Farrera et al. 1999) and lake status data indicating changes in runoff (Farrera et al. 1999; Kohfeld and Harrison 2000), show that most of the tropics and subtropics were very considerably drier at the LGM than today. This evidence is consistent with the reduction of precipitation associated with the ITCZ and the reduction of the strength of monsoonal circulations shown in the LGM simulation. The weakening of the surface winds over the Arabian Sea, which results in a reduction in monsoonal precipitation over India in our LGM simulation, is supported by evidence for weaker upwelling (Overpeck et al. 1996).

5.2 Europe and western Siberia

The coupled model results are also compared with the paleoclimate reconstructions from pollen records (Peyron et al. 1998; Tarasov et al. 1999) and the PMIP simulations (Kageyama et al. 2001) in Europe and western Siberia. The warmer climate over Western Europe, than indicated by both the pollen estimates and the PMIP simulations, is obtained by coupled LGM simulation during winter (Fig. 23a) mainly because the simulated SSTs in the North Atlantic at the LGM is warmer than that in the PMIP simulations. The anomalous cyclonic circulation that develops in the midlatitude eastern North Atlantic during winter (Fig. 16b) also contributes to the simulated warmer condition in Western Europe. This enhanced westerly flow advects a warm maritime air mass into Western Europe. The annual surface temperature change over Western Europe, however, shows a better agreement

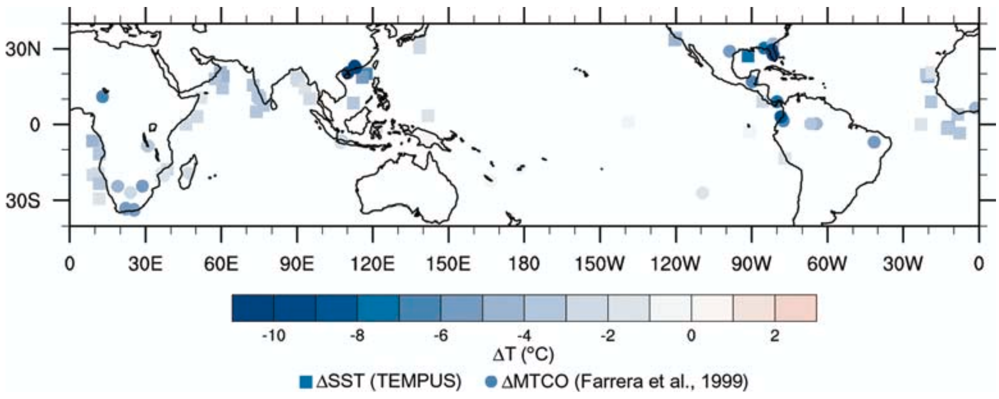

Fig. 22 Reconstructed changes in temperature at sea level, based on lowland sites and the application of regionally specific lapse rates, across the tropics at the LGM. The data are derived from Farrera et al. (1999). Alkenone-based reconstructions of SST changes in the tropics, derived from the TEMPUS data set (Rosell-Melé et al. 1998) are also plotted for comparison with the land-based estimates

Table 5 Glacial-age changes in mean temperature of the coldest month (ΔMTCO, °C) over key regions defined by Pinot et al. (1999a). The regions are: equatorial South America (50–75°W, 10°N–2°S), equatorial East Africa (25–45°E, 10°N–10°S), New Guinea (130–150°E, 0–10°S), subtropical South Africa (15–35°E, 15–30°S) and subtropical eastern North America (75–85°W, 30–35°N). The changes in coldest month temperature are inferred from vegetation data at selected locations within the regions mentioned (Farrera et al. 1999). The Minimum and Maximum of paleodata represent the minimum and maximum ΔMTCO within the regions respectively. The results of PMIP simulations (Pinot et al. 1999a) are average of eight PMIP models with prescribed SSTs and eight PMIP models with mixed-layer ocean. The simulated ranges of ΔMTCO are also given in parentheses. Detailed descriptions of PMIP models are in Pinot et al. (1999a). The coupled model, NCAR-CCSM, results are area-averaged ΔMTCO of regions mentioned

ΔMTCO	PALEODATA		PMIP SIMULATIONS		NCAR-CCSM
	(Farrera et al. 1999)		(average and range of 8 models)		(area-average)
	Minimum	Maximum	CLIMAP SSTs	Mixed-layer ocean	Coupled model
Equatorial South America	–3.0	–8.0	–2.0 (–1.0 to –3.0)	–3.0 (–1.0 to –4.5)	–3.5
Equatorial East Africa	–3.0	–5.0	–3.0 (–2.0 to –4.0)	–3.0 (–1.0 to –5.0)	–3.5
New Guinea	–2.0	–7.0	–2.0 (–0.5 to –5.0)	–3.0 (–1.0 to –5.5)	–3.6
Subtropical South Africa	–3.7	–6.5	–3.0 (–2.0 to –3.5)	–2.5 (–0.5 to –5.0)	–5.0
Subtropical eastern North America	–7.5	–15.5	–7.0 (–4.0 to –10.0)	–10.5 (–7.0 to –15.0)	–4.4

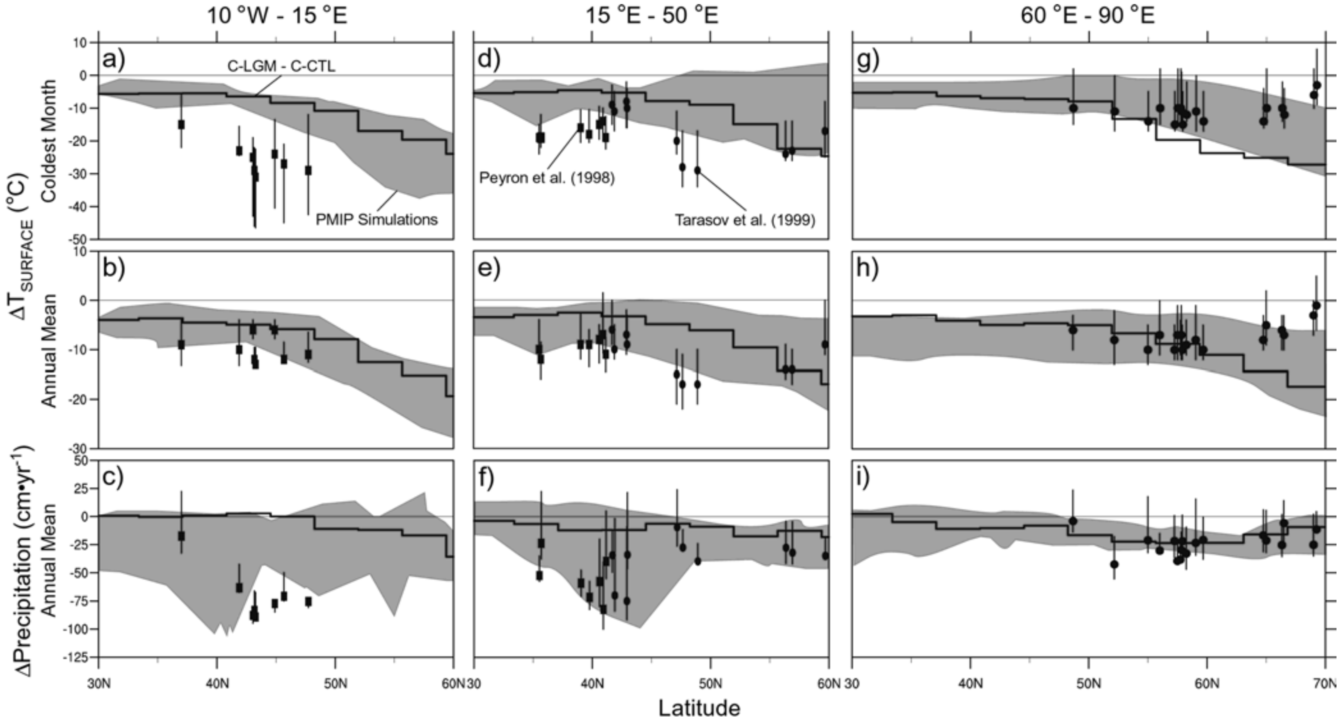

Fig. 23 The glacial-modern changes in zonally averaged **a** land surface temperature in the coldest month (°C), **b** annual land surface temperature (°C), and **c** annual precipitation change (cm·yr^{-1}) over Western Europe (10°W–15°E); **d**–**f** and **g**–**i** are the same as **a**-**b**, but for Central Europe (15–50°E) and western Siberia (60–90°E) respectively. The *line* represents the coupled model results, C-LGM C-CTL. The available pollen records over each region are also plotted (*closed circles* and *squares* represent the data from Peyron et al. 1998 and Tarasov et al. 1999 respectively). The ranges of LGM climate change from PMIP simulations (Kageyama et al. 2001) are also indicated by *gray shading*

with both the pollen records and the PMIP simulations (Fig. 23b). The coupled simulations underestimate the annual precipitation change over Western Europe compared to both the pollen estimates and the PMIP simulations (Fig. 23c). In Central Europe (Fig. 23d–f), the same disagreement appears with much improvement than that of Western Europe. In western Siberia, the simulated climate shows good agreement with both the paleoreconstructions and the PMIP simulations (Fig. 23g–i).

6 Concluding remarks

The NCAR-CCSM, a coupled dynamical model of the atmosphere, ocean, and sea-ice, is used to simulate the climate of the LGM in response to changes in the height and extent of glaciers, land–sea distributions, greenhouse gas concentrations and orbital parameters. The results show a cooling of about 3 °C over the tropical land surface and about 2 °C in the tropical ocean, with half of the changes contributed by reduced greenhouse gases at the LGM. In addition to greenhouse gas reduction, the positive water-vapor feedback and the enhanced ocean ventilation of the thermocline and the intermediate waters mainly from the Southern Ocean (Liu et al. 2001) may explain the other half of tropical cooling. In contrast to CLIMAP SSTs, cooling also occurs in the subtropical ocean, which is, in part, due to lowered greenhouse gases and atmosphere-ocean interaction. SSTs are cooled by up to 8 °C in the midlatitudes.

The simulation provides the estimates of the coupled dynamical response of the ocean to the LGM boundary conditions. The oceanic overturning circulation at the LGM appears not only shallower, but also weaker than the modern condition. These deep circulation changes are attributable to the increased surface density flux in the Southern Ocean caused by sea-ice expansion at the LGM. The intensified zonal wind stress along with the poleward shift of maximum stress in the Southern Ocean enhances the transport of ACC up to 50%. Both the Gulf Stream and the Kuroshio are intensified due to the overall increase of wind stress and, in turn, wind stress curl in the subtropical oceans. The changes of SSS are characterized by ubiquitous freshening relative to the salinity increase imposed as a boundary condition, except in the sea-ice covered regions. The increase in salinity under the sea-ice is mainly due to the release of brine during sea-ice formation. The simulated SSS in the Nordic seas at LGM is less than present but is more than present in the south of Greenland; this is where NADW forms in the LGM simulation.

Due to the sharp SST gradient that develops in the midlatitudes, the subtropical to midlatitude storm track precipitation is increased. The largest land surface cooling, over 20 °C, appears on the major ice-sheets during winter. The water content of the entire atmospheric column is decreased with maximum changes in the lower troposphere. The monsoon rainfall during the LGM is reduced in all monsoon regions including India, North Africa, southwest US/Mexico and southeastern China.

In zonal average, the simulated climate accords fairly well with most reconstructed climate changes within estimation uncertainties. The simulation shows two important differences from the CLIMAP reconstructions of SSTs. One is the absence of subtropical oceanic warming in the simulations. The warm SST anomalies estimated from foraminiferal data in the subtropical Pacific are replaced by 2–2.5 °C cooling in the coupled simulations. The second difference is the simulation of warmer conditions than CLIMAP in the northern midlatitude oceans, associated with reduced sea-ice cover. In both cases, more recent reconstructions (based on alkenones for the subtropics and dinoflagellate assemablges for the North Atlantic) are broadly consistent with the simulation and in conflict with CLIMAP. Similarly, land-based reconstructions of low-elevation changes in the tropics and subtropics support the zonally averaged changes shown in the simulation. In Europe and western Siberia, the simulated results underestimate the wintertime cooling and the annual precipitation change in the regions of oceanic influence, but better agreement in the inland areas. The simulated seasonal extent of sea-ice in the North Atlantic lies between two extreme reconstructions, the extensive sea-ice shown by CLIMAP and the more open condition shown by dinoflagellate assemblages. In the Southern Ocean, the simulated seasonal fluctuation of the sea-ice margin is increased compared to the CLIMAP reconstructions but broadly consistent with more recent reconstructions based on diatoms.

East–west patterns in both sea and land temperatures are less successfully simulated; the simulation tends to produce a zonal cooling that is too uniform. This suggests that other unconsidered factors with potentially regionally heterogeneous climatic effects, such as vegetation feedbacks and aerosol forcing, may be at work. Pollen and plant macrofossil data (e.g., Prentice et al. 2000) indicate a substantial decrease in forest cover at the LGM and a corresponding increase in high-albedo desert, steppe and tundra vegetation. Such vegetation changes would significantly impact on the LGM climates (Levis et al. 1999). These changes have been implicated (e.g., Mahowald et al. 1999) as the major cause of the observed increase in atmospheric dust loading (2–5 fold increase globally, with up to 20-fold increase in high latitudes: Kohfeld and Harrison 2000; Kohfeld and Harrison in press). Radiative calculations using realistic LGM dust fields (Mahowald et al. 1999) and optical properties suggest that a change in atmospheric dust loading of this magnitude could have produced a change in top-of-the-atmosphere forcing of about –2 to –3 $W \cdot m^{-2}$ in the tropics (Harrison et al. in press; Claquin et al. submitted), with large regional heterogeneity due to the uneven distribution of dust and the differing radiative effect of absorbing aerosols over land and ocean. Further investigations on the direct and indirect impacts of land-surface changes are thus required to improve our understanding of LGM climates. The ability to perform fully prognostic simulations of the major observed features of glacial-interglacial changes in the coupled ocean-atmosphere system, as demonstrated here, is the essential first step in this direction.

Acknowledgements The simulations were carried out during SS's visit to NCAR-CGD. We thank Ms. Christine Shields and Dr. Caspar Ammann for helping SS in the initial setup of CCSM,

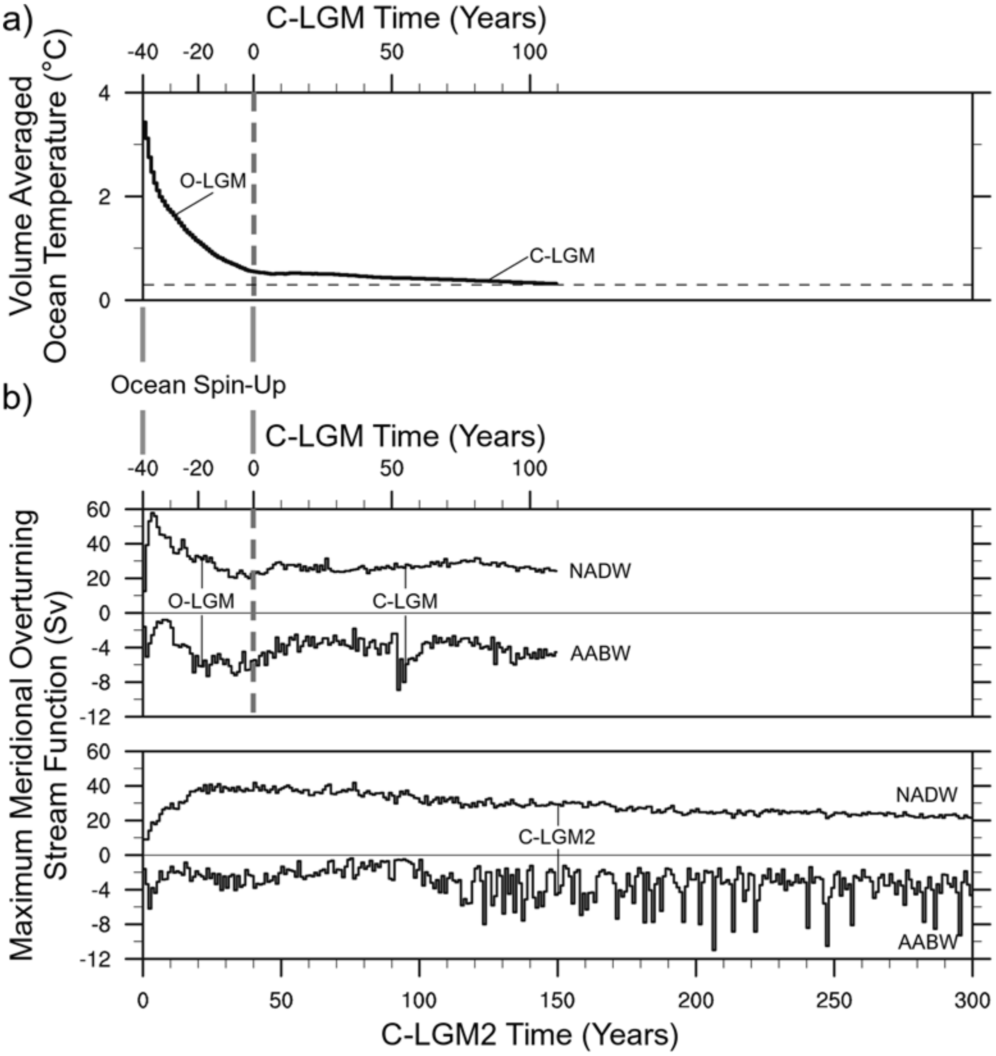

Fig. 24 The time series of **a** volume averaged ocean temperature (°C) of the C-LGM with ocean spin-up integration (O-LGM) and **b** meridional overturning stream function (Sv) of C-LGM with ocean spin-up integration (O-LGM) (*upper panel*) and C-LGM2 (*lower panel*)

Dr. Samuel Levis for sharing expertise on the LSM and Drs. Arne Winguth, Paul Loubere and Uwe Mikolajewicz for discussions on the climate of LGM. We also thank Mr. Will Lewis and Ms. Dong Eun Lee for editorial help. The comments from Dr. Karl Taylor of PCMDI and two anonymous reviewers contributed greatly to the revision of the paper. This work was supported by a grant from the NSF (ATM-9905285) to the University of Wisconsin-Madison and by a computer-time grant from the National Center for Atmospheric Research (NCAR), Boulder, CO. This is Center for Climatic Research, University of Wisconsin-Madison, USA, contribution number 766.

Appendix 1

Convergence of the coupled LGM simulation

The time series of the volume averaged ocean temperature in C-LGM is shown in Fig. 24a. Although the temperature change is still occurring, the rate of temperature change is very small over the last 50 years, 0.002 °C·yr^{-1}. This change is mainly because of the large adjustment time-scale of the deep-ocean state.

To investigate the sensitivity of coupled LGM simulations to the initial ocean states we integrated another coupled LGM simulation (C-LGM2) started from the modern ocean state (initial ocean state of C-CTL) for 300 surface model years with a deep-ocean acceleration technique (Bryan 1984) equivalent to the 15,000 abyssal years. Two LGM simulations, C-LGM and C-LGM2, produced a remarkably similar climate both in the ocean and in the atmosphere (Liu et al. 2002; Shin 2002). For example, two LGM simulations converge to a remarkably similar final meridional overturning strength (about 20 Sv of NADW and about 4 Sv of AABW) (Fig. 24b). This similarity between two LGM simulations, C-LGM and C-LGM2, including the meridional overturning strength regardless to the initial ocean state indicates the robustness of our coupling procedures used in this study.

References

Adams JM, Faure H (1997) Preliminary vegetation maps of the world since the Last Glacial Maximum: an aid to archaeological understanding. J Archaeol Sci 24: 623–647

Anderson D, Prell W, Barrat N (1989) Estimates of sea surface temperature in the Coral Sea at the last glacial maximum. Paleoceanography 4: 615–627

Andreasen DJ, Ravelo AC (1997) Tropical Pacific Ocean thermocline depth reconstructions for the Last Glacial Maximum. Paleoceanography 12: 395–414

Bard E, Rostek F, Sonzogni C (1997) Interhemispheric synchrony of the last deglaciation inferred from alkenone paleothermometry. Nature 385: 707–710

Berger AL (1978) Long-term variations of daily insolation and Quaternary climatic changes. J Atmos Sci 35: 2362–2367

Bigg GR, Wadley MR, Stevens DP, Johnson JA (1998) Simulations of two last glacial maximum ocean states. Paleoceanography 13: 340–351

Bonan GB (1998) The land surface climatology of the NCAR land surface model coupled to the NCAR community climate model. J Clim 11: 1307–1326

Boville BA, Gent PR (1998) The NCAR climate system model, version one. J Clim 11: 1115–1130

Broccoli AJ (2000) Tropical cooling at the Last Glacial Maximum: an atmosphere-mixed layer ocean model simulation. J Clim 13: 951–976

Broccoli AJ, Marciniak EP (1996) Comparing simulated glacial climate and paleodata: a reexamination. Paleoceanography 11: 3–14

Broecker WS (1995) The glacial world according to Wally. Eldigio Press, New York, USA, pp 318

Broecker WS, Peng T-H (1987) The oceanic salt pump: does it contribute to the glacial-interglacial difference in atmospheric CO_2 content? Global Biogeochem Cyc 1: 251–259

Broecker WS, Denton GH (1989) The role of ocean–atmosphere reorganizations in glacial cycle. Geochim Cosmochim Acta 53: 2465–2501

Broecker WS, Peteet DM, Rind D (1985) Does the ocean–atmosphere system have more than one stable mode of operation? Nature 315: 21–26

Bryan K (1984) Accelerating the convergence to equilibrium of ocean-climate models. J Phys Oceanogr 14: 666–673

Bush ABG, Philander SGH (1998) The ocean–atmosphere interactions in tropical cooling during the Last Glacial Maximum. Science 279: 1341–1344

Bush ABG, Philander SGH (1999) The climate of the Last Glacial Maximum: results from a coupled atmosphere–ocean general circulation model. J Geophys Res 104: 24,509–24,525

Chapman M, Shackleton N, Zhao M, Eglinton G (1996) Faunal and alkenone reconstructions of subtropical North Atlantic surface hydrography and paleotemperature over the last 28 kyr. Paloceanography 11: 343–357

CLIMAP project members (1976) The surface of the ice-age earth. Science 191: 1131–1137

CLIMAP project members (1981) Seasonal reconstructions of the of the earth's surface at the Last Glacial Maximum. Geological Society of America Map and Chart Series MC-36, pp 18

COHMAP Members (1988) Climate change of the last 18,000 years: observations and model simulations. Science 241: 1043–1052

Crosta X, Pichon J-J, Burckle LH (1998) Application of modern analogue technique to marine Antarctic diatoms: reconstruction of maximum sea-ice extent at the Last Glacial Maximum. Paleoceanography 13: 284–297

Crowley TJ, Baum SK (1997) Effect of vegetation on an ice-age climate model simulation. J Geophys Res 102: 16,463–16,480

de Vernal A, Rochon A, Turon J-L, Matthiessen J (1997) Organic-walled dinoflagellate cysts: palynological tracers of sea surface conditions in middle to high latitude marine environments. Geobios 30: 905–920

de Vernal A, Hillaire-Marcel C, Turon J-L, Matthiessen J (2000) Sea-surface conditions in middle to high latitudes of the North Atlantic during the last glacial maximum (LGM): the cold paradigm revisited. Can J Earth Sci (in press)

Dong B, Valdes PJ (1998) Simulations of the Last Glacial Maximum climates using a general circulation model: prescribed versus computed sea surface temperatures. Clim Dyn 14: 571–591

Doney SC, Large WG, Bryan FO (1998) Surface ocean fluxes and water-mass transformation rates in the coupled NCAR Climate System Model. J Clim 11: 1420–1441

Duplessy J-C, Shackleton NJ, Fairbanks RG, Labeyrie L, Oppo D, Kallel N (1988) Deepwater source variations during the last climatic cycle and their impact on the global deepwater circulation. Paleoceanography 3: 343–360

Duplessy J-C, Labeyrie L, Juillet-Leclerc A, Maitre F, Duprat J, Sarnthein M (1991) Surface salinity reconstruction of the North Atlantic Ocean during the last glacial maximum. Oceanol Acta 14: 311–324

Farrera I, Harrison SP, Prentice IC, Ramstein G, Guiot J, Bartlein PJ, Bonnefille R, Bush M, Cramer W, von Grafenstein U, Holmgren K, Hooghiemstra H, Hope G, Jolly D, Lauritzen S-E, Ono Y, Pinot S, Stute M, Yu G (1999) Tropical climates at the Last Glacial Maximum: a new synthesis of terrestrial paleoclimate data. I. vegetation, lake-levels and geochemistry. Clim Dyn 15: 823–856

Flato GM, Hilber WD (1992) Modelling pack ice as a cavitating fluid. J Phys Oceanogr 22: 626–651

Gates WL (1976) Modelling the ice-age climate. Science 191: 1138–1144

Ganopolski A, Rahmstorf S, Petoukhov V, Claussen M (1998) Simulation of modern and glacial climates with a coupled global model of intermediate complexity. Nature 391: 351–356

Gent PR, McWilliams JC (1990) Isopycnal mixing in the ocean circulation model. J Phys Oceanogr 20: 150–155

Gent PR, Willebrand J, McDougall TJ, McWilliams JC (1995) Parametrizing eddy-induced tracer transports in ocean circulation model. J Phys Oceanogr 25: 463–474

Gent PR, Bryan FO, Danabasoglu G, Doney SC, Holland WR, Large WG, McWilliams JC (1998) The NCAR climate system model global ocean component. J Clim 11: 1287–1306

Gent PR, Large WG, Bryan FO (2001) What sets the mean transport through Drake Passage? J Geophys Res 106: 2693–2712

Godfrey JS (1989) A Sverdrup model of the depth-integrated flow for the world ocean allowing for island circulations. Geophys Astrophys Fluid Dyn 45: 89–112

Guilderson TP, Fairbanks RG, Rubenstone JL (1994) Tropical temperature variations since 20,000 years ago: modulating inter-hemispheric climate change. Science 263: 663–665

Hall NMJ, Valdes PJ, Dong B (1996) The maintenance of the last great ice sheet: a UGAMP GCM study. J Clim 9: 1004–1019

Hansen JE, Lacis A, Ruedy R, Sato M, Wilson H (1993) How sensitive is the world's climate? Nat Geogr Res Explor 9: 143–158

Harrison SP, Kohfeld KE, Roelandt C, Claquin T (2001) The role of dust in climate changes today, at the last glacial maximum and in the future. Earth Sci Rev (in press)

Hoffert MI, Covey C (1992) Deriving global climate sensitivity from paleoclimate reconstructions. Nature 360: 573–576

Hewitt CD, Mitchell FB (1997) Radiative forcing and response of a GCM to ice age boundary conditions: cloud feedback and climate sensitivity. Clim Dyn 13: 821–824

Hewitt CD, Broccoli AJ, Mitchell JFB, Stouffer RJ (2001) A coupled model study of the last glacial maximum: was part of the North Atlantic relatively warm? Geophys Res Lett 28: 1571–1574

IPCC WG-I (1996) Climate change 1995: the science of climate change. In: Houghton et al (eds) Contribution of WGI to the second assessment report of the intergovernmental panel on climate change. Cambridge University Press, New York, pp 572

Janecek TR, Rea DK (1985) Quaternary fluctuations in the northern hemisphere trade winds and westerlies. Quat Res 24: 150–163

Joussaume S, Taylor KE, Braconnot P, Mitchell JFB, Kutzbach JE, Harrison SP, Prentice IC, Broccoli AJ, Abe-Ouchi A, Bartlein PJ, Bonfils C, Dong B, Guiot J, Herterich H, Hewitt CD, Jolly D, Kim JW, Kislov A, Kitoh A, Loutre MF, Masson V, McAvaney B, McFarlane N, de Noblet N, Peltier WR, Peterschmitt JY, Pollard D, Rind D, Royer JF, Schlesinger ME, Syktus J, Thompson S, Valdes P, Vettoretti G, Webb RS, Wyputta U (1999) Monsoon changes for 6000 years ago: results of 18 simulations from the Paleoclimate Modelling Intercomparison Project (PMIP). Geophys Res Lett 26: 859–862

Kageyama M, Peyron O, Tarasov P, Pinot S, Guiot J, Ramstein G, Joussaume S, PMIP participating groups (2001) The Last Glacial Maximum climate over Europe and western Siberia: a

PMIP comparison between models and data. Clim Dyn 17: 23–43

Kiehl JT, Hack JJ, Bonan GB, Boville BA, Williamson DL, Rasch PJ (1998) The national center for atmospheric research community climate model: CCM3. J Clim 11: 1131–1149

Kitoh A, Murakami S, Koide H (2001) A simulation of the Last Glacial Maximum with a coupled atmosphere–ocean GCM. Geophys Res Lett 28: 2221–2224

Klinck JM, Smith DA (1993) Effect of wind changes during the Last Glacial Maximum on the circulation in the Southern Ocean. Paleoceanography 8: 427–433

Kohfeld KE, Harrison SP (2000) How well can we simulate past climates? Evaluating the models using global palaeoenvironmental datasets. Quat Sci Rev 19: 321–346

Kohfeld KE, Harrison SP (2001) DIRTMAP: the geological record of dust. Earth Sci Rev (in press)

Kutzbach JE, Wright HE (1985) Simulations of the climate of 18,000 yr BP: results for the North American/North Atlantic/European sector and comparison with the geologic record. Quat Sci Rev 4: 147–187

Kutzbach JE, Guetter PJ (1986) The influence of changing orbital parameters and surface boundary conditions for the past 18,000 years. J Atmos Sci 43: 1726–1759

Large WG, McWilliams JC, Doney SC (1994) Oceanic vertical mixing: a review and a model with a nonlocal boundary layer parametrization. Rev Geophys 32: 363–403

Large WG, Danabasoglu G, Doney SC (1997) Sensitivity to surface forcing and boundary layer mixing in a global ocean model: annual-mean climatology. J Phys Oceanogr 27: 2418–2447

Lautenschlager M, Mikolajewicz U, Maier-Reimer E, Heinze C (1992) Application of ocean models for the interpretation of atmospheric general circulation model experiments on the climate of the Last Glacial Maximum. Paleoceanography 7: 769–782

Lea DW, Boyle EA (1990) Foraminiferal reconstruction of barium distributions in water masses of the glacial ocean. Paleoceanography 5: 719–742

Lee KE, Slowey NC (1999) Cool surface waters of the subtropical North Pacific Ocean during the last glacial. Nature 397: 512–514

Levis S, Foley JA, Pollard D (1999) CO_2, climate, and vegetation feedbacks at the Last Glacial Maximum. J Geophys Res 104: 31,191–31,198

Liu Z, Shin S, Behling P, Prell W, Trend-staid M, Harrison SP, Kutzbach JE (2000) Dynamical and observational constraints on tropical Pacific sea surface temperatures at the last glacial maximum. Geophys Res Lett 27: 105–108

Liu Z, Shin S, Otto-Bliesner B, Kutzbach JE, Brady EC (2001) Tropical cooling at the last glacial maximum and extratropical ocean ventilation. Geophys Res Lett (in press)

Lynch-Stieglitz J, Curry WB, Slowey N (1999) Weaker Gulf Stream in the Florida Straits during the Last Glacial Maximum. Nature 402: 644–648

Mahowald N, Kohfeld K, Hansson M, Balkanski Y, Harrison SP, Prentice IC, Schulz M, Rodhe H (1999) Dust sources and deposition during the last glacial maximum and current climate: a comparison of model results with paleodata from ice cores and marine sediments. J Geophys Res 104: 15,859–15,916

Manabe S, Hahn DG (1977) Simulation of the tropical climate of an ice age. J Geophys Res 82: 3889–3911

Mix AC, Morey AE, Pisias NG, Hostetler SW (1999) Foraminiferal faunal estimates of paleotemperature: circumventing the no-analog problem yields cool ice age tropics. Paleoceanography 14: 350–359

Moore Jr TC, Burckle LH, Geitzenauer K, Luz B, Molina-Cruz A, Robertson JH, Sachs H, Sancetta C, Thiede J, Thompson P, Wenkam C (1980) The reconstruction of sea surface temperatures in the Pacific Ocean of 18,000 BP. Mar Micropalaeontol 5: 215–247

Müller PJ, Kirst G, Ruhland G, von Storch I, Rosell-MeléA (1998) Calibration of the alkenone paleotemperature index [ ] based on core-tops from the eastern South Atlantic and the global ocean (60°N–60°S). Geochim Cosmochim Acta 62: 1757–1772

Müller A, Opdyke BN (2000) Glacial-interglacial changes in nutrient utilization and paleoproductivity in the Indonesian Throughflow sensitive Timor Trough, easternmost Indian Ocean. Paleoceanography 15: 85–94

Ohkouchi N, Kawamura K, Nakamura T, Taira A (1994) Small changes in the sea surface temperature during the last 20,000 years: molecular evidence from the western tropical Pacific. Geophys Res Lett 21: 2207–2210

Overpeck J, Anderson D, Trumbore S, Prell W (1996) The southwest Indian monsoon over the last 18,000 years. Clim Dyn 12: 213–225

Patrick A, Thunell RC (1997) Tropical Pacific sea surface temperatures and upper water column thermal structure during the last glacial maximum. Paleoceanography 12: 649–657

Peixoto JP, Oort AH (1992) Physics of climate. American Institute of Physics, New York, USA, pp 520

Peltier WR (1994) Ice age paleotopography. Science 265: 195–201

Peyron O, Guiot J, Cheddadi R, Tarasov P, Reille M, de Beaulieu J-L, Bottema S, Andrieu V (1998) Climatic reconstruction in Europe for 18,000 yr BP from pollen data. Quat Res 49: 183–196

Pinot S, Ramstein G, Harrison SP, Prentice IC, Guiot J, Stute M, Joussaume S (1999a) Tropical paleoclimates at the Last Glacial Maximum: comparison of paleoclimate modeling intercomparison project (PMIP) simulations and paleodata. Clim Dyn 15: 857–874

Pinot S, Ramstein G, Marsiat I, de Vernal A, Peyron O, Duplessy J-C, Weinelt M (1999b) Sensitivity of the European LGM climate to North Atlantic sea-surface temperature. Geophys Res Lett 26: 1893–1896

Prahl F, Pisias N, Sparrow M, Sabin A (1995) Assessment of sea surface temperature at 42°N in the California current over the last 30,000 years. Paleoceanography 4: 763–773

Prentice IC, Jolly D, BIOME 6000 Participant (2000) Mid-Holocene and glacial-maximum vegetation geography of the northern continents and Africa. J Biogeogr 27: 507–519

Raynaud D, Jouzel J, Barnola JM, Chappellaz J, Delmas RJ, Lorius C (1993) The ice record of greenhouse gases. Science 259: 926–934

Rea DK (1994) The paleoclimatic record provided by eolian deposition in the deep sea: the geologic history of wind. Rev Geophys 32: 159–195

Rind D, Peteet D (1985) Terrestrial conditions at the last glacial maximum and CLIMAP sea-surface temperature estimates: are they consistent? Quat Res 24: 1–22

Rochon A, de Vernal A, Sejrup H, Haflidason H (1998) Palynological evidence of climatic and oceanographic changes in the North Sea during the last deglaciation. Quat Res 49: 197–207

Rosell-Melé A, Koc N (1997) Paleoclimatic significance of the stratigraphic occurrence of phytosynthetic biomarker pigments in the Nordic Seas. Geology 49–52

Rosell-Melé A, Bard E, Emeis K-C, Farrimond P, Grimalt J, Müller PJ, Schneider RR (1998) TEMPUS: a new generation of sea surface temperature maps. Eos Trans Am Geophys Union 79: 393–394

Sarnthein M, Tetzlaff G, Koopmann B, Wolter K, Pflaumann U (1981) Glacial and interglacial wind regimes over the eastern subtropical Atlantic and North-West Africa. Nature 293: 193–196

Sawada K, Handa N (1998) Variability of the path of the Kuroshio ocean current over the past 25,000 years. Nature 392: 592–595

Schmitt RW, Bogden PS, Dorman CE (1989) Evaporation minus precipitation and density fluxes for the North Atlantic. J Phys Oceanogr 19: 1208–1221

Seidov D, Sarnthein M, Stattegger K, Prien R, Weinelt M (1996) North Atlantic Ocean circulation during the last glacial maximum and subsequent meltwater event: a numerical model. J Geophys Res 101: 16,305–16,332

Seidov D, Haupt BJ (1997) Simulated ocean circulation and sediment transport in the North Atlantic during the last glacial maximum and today. Paleoceanography 12: 281–305

Semtner AJ (1976) A model for the thernodynamic growth of sea-ice in numerical investigations of climate. J Phys Oceanogr 6: 376–389

Shea DJ, Trenberth KE, Raynolds RW (1990) A global monthly sea surface temperature climatology. NCAR Technical note NCAR/TN-345+STR, Colorado, pp 167

Shin S (2002) Understanding the climate of the Last Glacial Maximum using a climate system model. PhD Thesis at the University of Wisconsin-Madison, USA, pp 175

Slowey NC, Curry WB (1992) Enhanced ventilation of the North Atlantic subtropical gyre thermocline during the last glaciation. Nature 358: 665–668

Sonzogni C, Rostek EBF, Dollfus D, Rosell-MeléA, Eglinton G (1997) Alkenones in recent surface sediments from the subtropical and Indian Ocean. Quat Res 47: 344–355

Speer K, Tziperman E (1992) Rates of water mass formation in the North Atlantic Ocean. J Phys Oceanogr 22: 93–104

Tarasov PE, Peyron O, Guiot J, Brewer S, Volkova VS, Bezusko LG, Dorofeyuk NI, Kvavadze EV, Osipova IM, Panova NK (1999) Last Glacial Maximum climate of the former Soviet Union and Mongolia reconstructed from pollen and plant macrofossil data. Clim Dyn 15: 227–240

Trend-Staid M (1999) Sea-surface temperature and near-surface hydrography at the Last Glacial Maximum: A reconstruction using modern analogue technique. PhD Thesis at Brown University, USA, pp 319

Wetherly JW, Briegleb BP, Lovge WE, Muslanik JA (1998) Sea ice and polar climate in the NCAR-CSM. J Clim 11: 1472–1486

Weaver AJ, Eby M, Fanning AF, Wiebe EC (1998) Simulated influence of carbon dioxide, orbital forcing and ice-sheets on the climate of the Last Glacial Maximum. Nature 394: 847–853

Webb RS, Rind DH, Lehman SJ, Healy RJ, Sigman D (1997) Influence of ocean heat transport on the climate of the Last Glacial Maximum. Nature 385: 695–699

Weinelt M, Sarnthein M, Pflaumann U, Schulz H, Jung S, Erlenleuser H (1996) Ice-free Nordic Seas during the last glacial maximum? Potential sites of deepwater formation. Paleoclimate 1–4: 283–309

Whitworth III T (1983) Monitoring the transport of the Antarctic Circumpolar Current at Drake Passage. J Phys Oceanogr 13: 2045–2057

Winguth AME, Archer D, Duplessy J-C, Maier-Reimer E, Mikolajewicz U (1999) Sensitivity of paleonutrient tracer distributions and deep-sea circulation to glacial boundary conditions. Paleoceanography 14: 304–323

Wolff T, Mulitza S, Arz H, Patzold J, Wefer G (1998) Oxygen isotopes versus CLIMAP (18 ka) temperatures: a comparison from the tropical Atlantic. Geology 26: 675–678

Zhao M, Beveridge N, Shackleton N, Sarnthein M, Eglinton G (1995) Molecular stratigraphy of cores off northwest Africa: sea surface temperature history over the last 80 ka. Paleoceanography 10: 661–675